



A new deep learning-based model for reconstructing high-quality NDVI time-series data in heavily cloudy areas: fusion of Sentinel 1 and 2 data

Yang Chen, Ruyin Cao, Shuaijun Liu, Longkang Peng, Xuehong Chen & Jin Chen

To cite this article: Yang Chen, Ruyin Cao, Shuaijun Liu, Longkang Peng, Xuehong Chen & Jin Chen (2024) A new deep learning-based model for reconstructing high-quality NDVI time-series data in heavily cloudy areas: fusion of Sentinel 1 and 2 data, International Journal of Digital Earth, 17:1, e2407941, DOI: [10.1080/17538947.2024.2407941](https://doi.org/10.1080/17538947.2024.2407941)

To link to this article: <https://doi.org/10.1080/17538947.2024.2407941>



© 2024 The Author(s). Published by Informa UK Limited, trading as Taylor & Francis Group



[View supplementary material](#)



Published online: 07 Oct 2024.



[Submit your article to this journal](#)



Article views: 820



[View related articles](#)



[View Crossmark data](#)



A new deep learning-based model for reconstructing high-quality NDVI time-series data in heavily cloudy areas: fusion of Sentinel 1 and 2 data

Yang Chen^{a,c}, Ruyin Cao^b, Shuaijun Liu^a, Longkang Peng^a, Xuehong Chen^a and Jin Chen^a

^aState Key Laboratory of Earth Surface Processes and Resource Ecology, Institute of Remote Sensing Science and Engineering, Faculty of Geographical Science, Beijing Normal University, Beijing, People's Republic of China;

^bSchool of Resources and Environment, University of Electronic Science and Technology of China, Chengdu, People's Republic of China; ^cAerospace Information Research Institute, Chinese Academy of Sciences, Beijing, People's Republic of China

ABSTRACT

Reconstructing high-quality Normalized Difference Vegetation Index time series data is essential for ecological and agricultural applications but remains challenging in heavily cloudy areas. Fusing Sentinel SAR and optical data with deep learning could be helpful but is also challenging for stable models due to unstable SAR-NDVI relationships caused by imaging mechanism differences and environmental complexities. In this study, we developed a new Bidirectional Recurrent Imputation for Optical-SAR fusion (BRIOS) model to reconstruct high-quality Sentinel-2 NDVI time series data. BRIOS designs a two-layer recurrent architecture that integrates the autocorrelation of discrete, cloud-free NDVI observations into the model for a more stable SAR-NDVI relationship. Evaluating BRIOS against three baseline methods (GF-SG spatiotemporal fusion, Harmonic regression interpolation, and MCNN-Seq deep learning) across three full Sentinel-2 tiles in reconstructing 8-day NDVI time series, BRIOS consistently outperformed in scenarios of either random or continuously missing data, as evidenced by lower RMSE values (e.g. 0.075 for BRIOS vs. 0.108 for GF-SG vs. 0.143 for Harmonic regression vs. 0.303 for MCNN-Seq), better Edge index, and high linear correlation coefficients (R values up to 0.97). Further ablation experiments revealed that deep integration of NDVI autocorrelation features and SAR temporal change patterns has improved the stability and generalization of BRIOS. Discussions on the model's scalability across various cloud sizes and training dataset sizes affirm its practicality for broad-scale application in vegetation monitoring under challenging cloudy conditions.

ARTICLE HISTORY

Received 1 April 2024

Accepted 18 September

2024

KEYWORDS

NDVI time-series data; Synthetic Aperture Radar data; Recurrent Neural Networks (RNN); heavily cloudy areas; Sentinel 1/2

1. Introduction

The Normalized Difference Vegetation Index (NDVI) is the most common proxy for canopy greenness and vigor in the field of remote sensing (Delbart et al. 2006; Huete et al. 2002; Rouse et al. 1974). Accordingly, NDVI time-series data have been commonly used in monitoring ecosystem

CONTACT Jin Chen ✉ chenjin@bnu.edu.cn 📧 Institute of Remote Sensing Science and Engineering, Faculty of Geographical Science, Beijing Normal University, Beijing 100875, People's Republic of China

📄 Supplemental data for this article can be accessed online at <https://doi.org/10.1080/17538947.2024.2407941>.

© 2024 The Author(s). Published by Informa UK Limited, trading as Taylor & Francis Group

This is an Open Access article distributed under the terms of the Creative Commons Attribution-NonCommercial License (<http://creativecommons.org/licenses/by-nc/4.0/>), which permits unrestricted non-commercial use, distribution, and reproduction in any medium, provided the original work is properly cited. The terms on which this article has been published allow the posting of the Accepted Manuscript in a repository by the author(s) or with their consent.

dynamics and modeling biosphere processes to help understand ecosystem responses to climate change (Pettorelli et al. 2005; Zeng et al. 2022). Unfortunately, current satellite sensors still lack the ability to provide high-spatiotemporal-resolution NDVI data because of the trade-off between spatial and temporal resolution (Gao et al. 2006). Accordingly, the available global NDVI time-series products (e.g. GIMMS, MODIS, SPOT VGT) usually suffer from two problems that prevent them from fully satisfying the requirements of these applications. One is their coarse spatial resolution, which ranges from 250 m to 8 km and greatly hinders their application in heterogeneous landscapes (Gao et al. 2006; Rao et al. 2015). The second is that they are quite discontinuous in time because of frequent cloud contamination, particularly in heavily cloudy areas (Chen et al. 2004; Pettorelli et al. 2005). The first problem has been greatly mitigated by the recent emergence of CubeSat constellations and new satellite systems (e.g. Sentinel 2 data with five-day or shorter revisit cycles and 10-m spatial resolution), and high-spatial-resolution NDVI time-series data are beginning to be available based on Sentinel-2 data or Harmonized Landsat and Sentinel-2 (HLS) data (Claverie et al. 2018). Regarding the second problem of discontinuous data in NDVI time series, although various methods have been developed to address this problem (e.g. Carrao, Gonçalves, and Caetano 2009; Fisher, Mustard, and Vadeboncoeur 2006; Gao et al. 2006; Yan and Roy 2018; Zhu et al. 2018), this problem is still imperfectly solved, especially in heavily cloudy areas where cloudy skies can persist for long periods and affect all optical satellite sensors simultaneously. This reduces the effectiveness of all existing methods (Chen et al. 2021; Jia et al. 2011; Yan and Roy 2020). Combining cloud-free Synthetic Aperture Radar (SAR) data with optical data is considered a promising option to overcome this problem and reconstruct high-quality NDVI time series data with high spatiotemporal resolution.

Previous studies have proposed three types of methods for reconstructing high spatiotemporal resolution NDVI time-series data. The first method is based on temporal interpolation, which fits the Landsat or Sentinel-2 NDVI time-series data with various mathematic functions, such as a logistic model (Melaas, Friedl, and Zhu 2013), a Fourier analysis model (such as HANTS) (Roerink, Menenti, and Verhoef 2000; Zhou, Jia, and Menenti 2015), a Savitzky–Golay filter (Cao et al. 2018; Chen et al. 2021; Chen et al. 2004), linear harmonic models (Wilson, Knight, and McRoberts 2018; Yan and Roy 2018; Zhu et al. 2015), and nonlinear harmonic models (Carrao, Gonçalves, and Caetano 2009; Roy and Yan 2020). The performance of temporal interpolation methods depends not only on whether the actual NDVI dynamics are consistent with the assumptions of different fitting functions but also strongly on the number of cloud-free Landsat/Sentinel-2 observations and their temporal distribution. The second type of method is the well-known spatiotemporal fusion method that blends data from different satellite sensors. An example would be blending Landsat/Sentinel-2 observations with MODIS data to generate Landsat (Sentinel-2)-like NDVI time-series data (Chen et al. 2021; Claverie et al. 2018; Liu et al. 2019; Qiu et al. 2021; Rao et al. 2015; Wang et al. 2022). However, the performance of spatiotemporal fusion is substantially affected by differences in the spatial resolution of different sensors (Chen et al. 2021; Zhou et al. 2021), the number of cloud-free Landsat/Sentinel-2 observations, and their temporal distribution. In heavily cloudy areas, the long-term absence of valid Landsat/Sentinel-2 and MODIS observations significantly reduces the effectiveness of all fusion methods (Chen et al. 2020).

Synthetic Aperture Radar (SAR) has the advantage of penetrating cloud layers. More importantly, SAR records backscatter information from the land surface that has also been shown to reflect the dynamics of vegetation growth (Fauvel et al. 2020; Minh et al. 2018; Villarroya-Carpio, Lopez-Sanchez, and Engdahl 2022; Vreugdenhil et al. 2018). A promising third method for reconstructing optical images in cloudy areas is therefore to blend optical data with SAR data. With the release of free Sentinel-1 C-band SAR data, an increasing number of studies have focused on the fusion of Sentinel-2 optical data and Sentinel-1 SAR data. For example, some studies have used the framework of spatiotemporal fusion technology and simulated a Sentinel-2 optical image for a discrete prediction date by using Sentinel-1 SAR images for the prediction date and optical and SAR image pairs for other dates (Ebel et al. 2020; Gao et al. 2020; Scarpa et al. 2018). Zhao

et al. (2020) have further proposed a new method to reconstruct cloud-free NDVI time-series data through the fusion of Sentinel-1 and Sentinel-2 time-series data, instead of simulating a single Sentinel-2 optical image. Their method, referred to as Multi-CNN-Sequence to Sequence (MCNN-Seq), approximates the relationship between optical and SAR sequences with a deep learning model. Li et al. (2022) followed this idea to learn the complex SAR-NDVI relationship with the Transformer model (TTSM). To reduce the influence of SAR noise on optical-SAR fusion, Garioud et al. (2021) further jointly integrated multivariate SAR and NDVI time series at the parcel scale. However, this method (SenRVM) is difficult to apply in fragmented croplands and areas without reliable ancillary parcel data.

Optical NDVI and SAR signals have different imaging mechanisms. NDVI reflects mainly leaf chlorophyll and vegetation coverage/LAI, whereas SAR backscattering information is more related to vegetation canopy structure and water content in the vegetation canopy and soil background. The fact that the relationship between the two signals is therefore often indirect and spatiotemporally unstable makes it difficult to precisely capture the relationship with a fixed regression model. Recent studies, such as MCNN-Seq, SenRVM, and TTSM, have adopted data-driven, deep learning models to simulate such complex relationships (Garioud et al. 2021; Li et al. 2022; Scarpa et al. 2018; Zhao et al. 2020). As shown in Figure 1, these methods attempted to directly transfer SAR time series data to predicted NDVI time series data. They focus more on fully exploiting SAR data to obtain deep temporal features and then establishing a direct mapping relationship between SAR and NDVI data. Continuous and complete NDVI time series data are necessary to supervise these models to obtain reliable reference information on the SAR-NDVI mapping relationship. In other words, NDVI observations are used only to calculate the loss function rather than as direct input variables in the models. The autocorrelation features implied by the NDVI time series data itself, i.e. current NDVI values are correlated with cloud-free NDVI observations in time series, have not been fully used. As a result, the temporal dynamics of NDVI observations have been underestimated by previous SAR-optical fusion models, and this underestimation may have led to two limitations. First, previous methods may not be effective when temporal changes of SAR data are inconsistent with those of the local discrete optical data due to the differences in the imaging mechanisms between them and complex environmental interferences. Secondly, due to the unstable

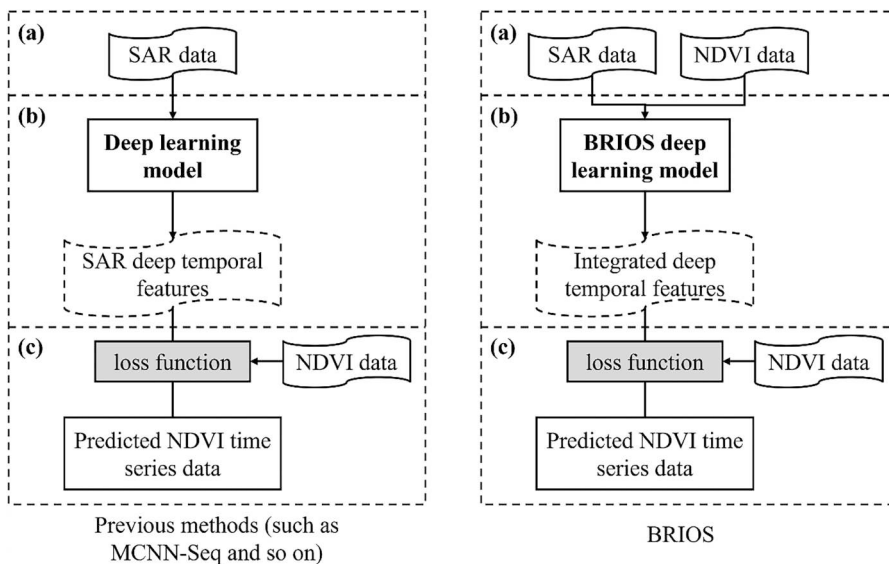


Figure 1. Overview of previous deep learning-based SAR-fusion methods and BRIOS. (a) input variables; (b) feature processing; (c) model training and predicting.

relationships between SAR sequences and NDVI time-series data, previous methods require nearly complete NDVI time-series data as training labels to supervise the model's ability to correctly predict values for each date. However, the use of incomplete NDVI time series to train SAR-optical fusion models is sometimes problematic in the presence of frequent cloud cover. The influence of varying degrees of incomplete NDVI data on the model's performance has not been thoroughly examined. Considering the benefits of using the autocorrelation of NDVI time series as an input to predict missing NDVI data, even when the NDVI time series are discontinuous in time (Cao et al. 2020; Chen et al. 2021), these two limitations are likely to be mitigated by making better use of the autocorrelation of NDVI time series from discrete NDVI observations and coordinating SAR and optical temporal information. In addition to the model structure, another concern about establishing a stable SAR-NDVI relationship is the quality of SAR data. SAR time-series data usually show abnormal fluctuations because of the influence of various environmental factors, such as sudden changes in surface humidity (Velooso et al. 2017; Vreugdenhil et al. 2018), topographic effects, and speckle noise caused by different targets interfering with each other within a pixel. Although some techniques, such as terrain correction and enhanced speckle filtering, have been used to remove SAR noise in the spatial domain, residual noise (e.g. anomalous fluctuations) still exists in SAR time-series data. It is still unclear whether and to what extent the SAR time series should be smoothed to establish a more robust relationship between NDVI and SAR signals.

Because of the above unresolved issues, we proposed a new deep learning-based model – Bidirectional Recurrent Imputation for Optical-SAR fusion (BRIOS) – to reconstruct high-quality Sentinel-2 NDVI time-series data. The main contributions of BRIOS are (1) using cloud-free NDVI data from partially cloud-contaminated images as direct input to fully utilize the inherent autocorrelation feature of NDVI time series to establish a more accurate SAR-NDVI relationship (Figure 1); (2) using Savitzky-Golay filter to extract the temporal variation pattern of SAR time series data and reduce the residual noise in the SAR time series data, thus improving the performance of SAR-NDVI fusion. It is expected that the inclusion of NDVI observations and the improvement of SAR data quality in BRIOS will enhance the stability and generalization of the SAR-NDVI relationship over large regions with complex landscapes. To verify this, we tested BRIOS's applicability across large regions like the three Sentinel-2 tiles and compared the results with those of existing baseline methods. Furthermore, we delved deeper into the BRIOS model's sensitivity to several factors such as input variables, cloud size, and the size of the training dataset, by conducting a variety of simulated experiments.

2. BRIOS method

Generally, the BRIOS method employs a two-layer bidirectional RNN architecture to fuse optical cloud-free NDVI observations and the temporal change patterns of SAR time-series data. Figure 2 shows the flowchart of BRIOS, which includes two main steps. First, the patterns of temporal change of SAR time-series data extracted by a wide-window Savitzky-Golay (SG) filter are used as the SAR input variables. The NDVI time series with missing data are used as both the inputs of the RNN architecture and for calibration of the loss function. Secondly, BRIOS designs a bidirectional RNN network with a two-layer recurrent architecture to get the temporal hidden-state features based on the SAR dynamics and the temporal dynamics from cloud-free NDVI observations. The regression layer thus converts the hidden-state features to the predicted NDVI values. In the following sections, we illustrate details regarding the input variables of BRIOS (section 2.1), the forward unidirectional recurrent imputation architecture (section 2.2), and the bidirectional recurrent imputation model (section 2.3).

2.1. The input variables of BRIOS

We used the $NDVI_{series} = \{ndvi_1, \dots, ndvi_i, \dots, ndvi_N\}$ to denote the input NDVI time-series data of N observations in a given year. All NDVI observations in the $NDVI_{series}$ have the

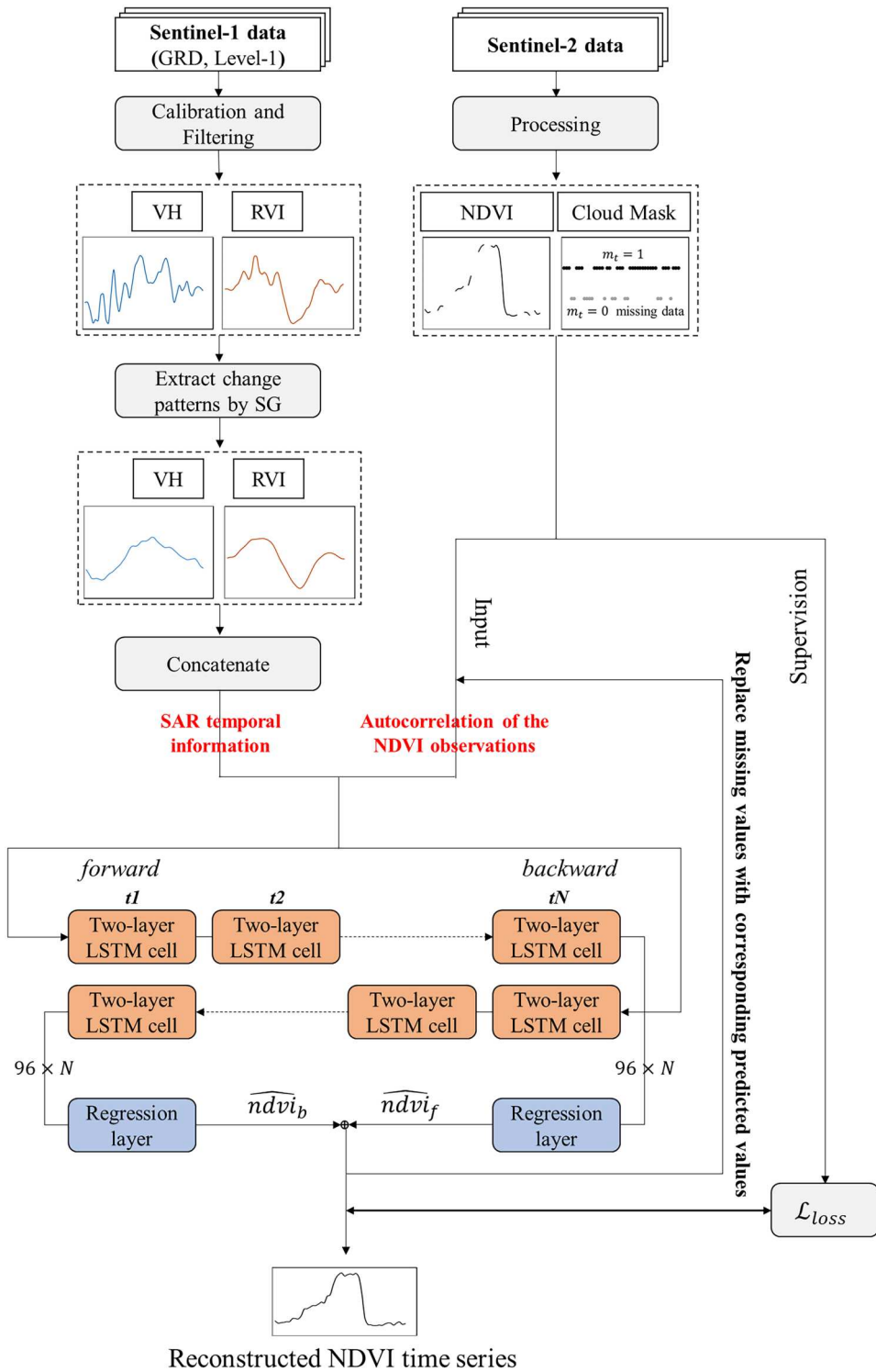


Figure 2. Flowchart of the BRIOS method.

corresponding data quality flags m_t , in which missing values (no valid observations due to cloud contamination) and valid observations are labeled as 0 and 1, respectively. We defined δ_t as the time interval between the date t and the date of the last cloud-free NDVI observation before t , expressed as:

$$\delta_t = \text{doy}_t - \text{doy}_{t-i} \quad (1)$$

where doy_t is the DOY (day of the year) of date t , and the doy_{t-i} is the DOY of the cloud-free observation at the i th time step before the date t .

For SAR data, we selected VH and Radar Vegetation Index (RVI) (See Equation 10) because they are consistent with vegetation growth or correlated well with vegetation biophysical parameters (Kim et al. 2011; Mandal et al. 2020; Nasirzadehdizaji et al. 2019). We did not include the VV backscatter data in our study because the VV signal is more susceptible to variations in topographic relief and multiple scattering interferences, and thus is less correlated with NDVI than the VH signal (Velooso et al. 2017; Periasamy, 2018). Since SAR signals are subject to multiple interferences, the relationship between a SAR signal and NDVI data is not stable throughout the growing season. To address this issue, we did not use the SAR time-series data directly. Instead, the temporal change patterns of the SAR data were used as the input variables in BRIOS. The annual change patterns of the VH and RVI time-series data were extracted by using the SG filter with a wide moving window and a low-degree polynomial. Following Chen et al. (2004), we determined the half-width of the moving window of the SG filter to be 6 (i.e. approximately one month) and the degree of the polynomial to be 2. The superiority of using the temporal change patterns is discussed in section 5.1.2. The extracted temporal change patterns of the VH and RVI time series were connected along the temporal axis as the input sequence vector $\text{SAR}_{\text{series}} = \{\text{sar}_1, \text{sar}_2, \dots, \text{sar}_{N-1}, \text{sar}_N\}$.

2.2. Unidirectional two-layer recurrent imputation architecture

We assumed that for the t -th step, the predicted NDVI ($\widehat{\text{ndvi}}_t$) was not only correlated with the current SAR observations (referred to as the feature correlation between SAR and NDVI data) but also correlated with discrete cloud-free NDVI observations in the time series itself (referred to as the autocorrelation of the NDVI time-series data). We proposed an imputation algorithm by unidirectional recurrent dynamics, which integrated the feature correlation of the SAR-NDVI and autocorrelation of the NDVI with the help of two recurrent architectures. Figure 3 shows the unidirectional recurrent imputation architecture, which consisted of the following components: (1) an

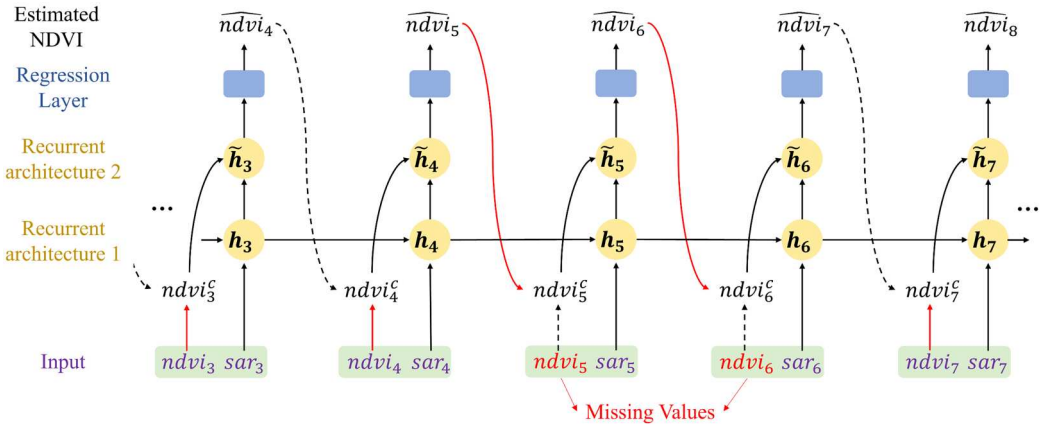


Figure 3. Unidirectional recurrent imputation architecture (forward direction). Suppose a NDVI time-series dataset $\text{NDVI}_{\text{series}} = \{\text{ndvi}_1, \dots, \text{ndvi}_t, \dots, \text{ndvi}_N\}$, where ndvi_5 and ndvi_6 are missing. According to the recurrent dynamics, at each date t , we can obtain a predicted $\widehat{\text{ndvi}}_t$ based on the hidden-state features and NDVI observations at the previous $t-1$ steps.

input layer composed of SAR and NDVI time-series data; (2) a two-layer recurrent architecture (i.e. the yellow module in Figure 3) that obtained the output hidden-state features \tilde{h}_t ; (3) the regression layer (i.e. the blue module in Figure 3) that transferred the hidden-state features \tilde{h}_t to the prediction value \widehat{ndvi}_t through a fully connected network as follows:

$$\widehat{ndvi}_t = W_x \tilde{h}_{t-1} + b_x \quad (2)$$

The solid lines in Figure 3 represent the paths through the network variables, and the dashed lines represent the paths that do not pass through the network variables. Next, we specifically introduced the working principle of the two-layer recurrent architecture.

In the two-layer recurrent architecture, the first recurrent architecture (h_t) extracts reliable temporal dynamics from the SAR temporal change patterns, and the second recurrent architecture (\tilde{h}_t) combines the SAR temporal dynamic features and cloud-free NDVI observations at the current t steps to get the output hidden-state features. These two recurrent architectures are achieved separately by the recurrent neural network. A standard recurrent network can be represented as follows (Goodfellow, Bengio, and Courville 2016):

$$H_t = \sigma(W_h H_{t-1} + U_h x_t + b_h) \quad (3)$$

where σ is the sigmoid function; W_h , U_h , and b_h are parameters; and H_{t-1} is the hidden-state features of previous time steps. At each time step, current hidden-state features depend on input data x_t and the previous hidden state H_{t-1} . The new two-layer architecture differs from prior works that used only recurrent dynamical architecture to learn features from SAR data or NDVI data alone. The new two-layer architecture therefore improves the representation of x_t and H_{t-1} by integrating both SAR and NDVI input data.

In the first recurrent architecture, we obtained h_t based on SAR temporal change patterns as the new representation of previous time steps:

$$h_t = \sigma(W_h h_{t-1} + U_h sar_t + b_h) \quad (4)$$

The variable h_t preserves the specific temporal dynamics features for the date t transmitted from the previous time steps. In previous self-imputation models (Li et al. 2021; Xiong et al. 2023), h_t was usually extracted from the NDVI time series itself. However, if there are long data gaps in the NDVI time-series data, the NDVI temporal profile is more difficult to reliably describe by h_t . Therefore, in the first recurrent architecture, consecutive SAR_{series} are used as indispensable auxiliary data to get a new h_t via Equation 4. By iterating Equation 4 during time steps, we integrated the SAR time-series data into the updating of recurrent dynamics, and we then substituted h_t into the second recurrent network to predict NDVI.

In the second recurrent architecture, because NDVI observations $ndvi_t$ may be missing values (i.e. $m_t = 0$), we could not use $ndvi_t$ as the input x_t of the standard recurrent network directly. Instead, we used the corresponding predicted values (i.e. \widehat{ndvi}_t) for the ‘complement’ input $ndvi_t^c$ when $ndvi_t$ was missing:

$$ndvi_t^c = m_t \times ndvi_t + (1 - m_t) \times \widehat{ndvi}_t \quad (5)$$

Formally, we used h_t as the previous hidden state and $ndvi_t^c$ as the input data of the second recurrent architecture. We then updated the model with Equation 6:

$$\tilde{h}_t = \sigma(W_{\tilde{h}}[h_t \times \gamma_t] + U_{\tilde{h}}[ndvi_t^c \circ m_t] + b_{\tilde{h}}) \quad (6)$$

where \circ indicates the concatenate operation, and $W_{\tilde{h}}$, $U_{\tilde{h}}$ and $b_{\tilde{h}}$ are parameters. Because the NDVI time series may be irregularly sampled because of random cloud contamination, we used the temporal decay factor γ_t (Che et al. 2018) to represent the missing patterns in the time series as

follows:

$$\gamma_t = \exp\{-\max(0, W_\gamma \delta_t + b_\gamma)\} \quad (7)$$

where δ_t is the time gap defined in Section 2.1.1, and W_γ and b_γ are parameters. A larger value of γ_t indicates that the previous time step is closer to the current date t , and the more it contributes to the calculation of the hidden-state features. During the iteration of Equation 6 over time, missing NDVI values are regarded as variables in the network, which are directly learned from SAR and NDVI synthetic temporal information (i.e. substituting Equation 4 into Equation 6) and effectively updated when the error is passed during backpropagation. For date t , if $ndvi_t$ is a cloud-free observation, it is used as a reference value in the loss function (Equation 8) to evaluate the imputed value, and this cloud-free $ndvi_t$ is passed to the next recurrent steps. Otherwise, we replaced $ndvi_t$ with a missing value with the predicted \widehat{ndvi}_t and passed \widehat{ndvi}_t to the next time-step. Because subsequent observations are correlated with the current value, we used the subsequent cloud-free observations to estimate the prediction error of the current \widehat{ndvi}_t as loss. For example, in Figure 3, the prediction errors of missing data $ndvi_5$ to $ndvi_6$ depend on the prediction error of cloud-free observations at the next (7-th) date. However, if $ndvi_5$ and $ndvi_6$ are treated as constants, the prediction errors of $ndvi_5$ and $ndvi_6$ cannot be fully back-propagated. To address this issue, we treated \widehat{ndvi}_t as a variable of the RNN (i.e. by substituting Equation 5 into Equation 6). The prediction errors could then be backpropagated along the opposite direction of solid lines to optimize the imputation accuracy.

2.3. Bidirectional recurrent imputation model

Typically, the prediction errors and convergence rates of unidirectional recurrent imputation architecture are inconsistent in different directions. To achieve robust predictions and avoid a bias-exploding problem, a bidirectional recurrent imputation model is needed to handle time-series data in both directions (Bengio et al. 2015). Two separate recurrent imputation architectures (details seen in Section 2.2) were used for the forward direction and the backward direction. The recurrent component in each architecture consisted of the long short-term memory (LSTM) with 96 hidden units. For each direction, we used the Mean Squared Error (MSE) as the loss function calculated by the following equation:

$$L = \frac{1}{N} \sum_{t=1}^N \ell_t, \quad \text{where } \ell_t = m_t(\widehat{ndvi}_t - ndvi_t)^2 \text{ at } t\text{-th date} \quad (8)$$

where N is the length of the time-series data. Only cloud-free NDVI observations were used to calculate the MSE. In the forward direction, we obtained the predicted sequence $\{\widehat{ndvi}_1, \widehat{ndvi}_2, \dots, \widehat{ndvi}_N\}$ and the loss sequence $\mathcal{L}_{forward} = \{\ell_1, \ell_2, \dots, \ell_N\}$. Similarly, in the backward direction, we obtained another predicted sequence $\{\widehat{ndvi}'_1, \widehat{ndvi}'_2, \dots, \widehat{ndvi}'_N\}$ and another loss sequence $\mathcal{L}_{backward} = \{\ell'_1, \ell'_2, \dots, \ell'_N\}$. To ensure predictions in each step were consistent in both directions, we further used a consistency loss \mathcal{L}_{cons} , which was calculated as the MSE value between the predictions of both directions (i.e. $|\widehat{ndvi}_t - \widehat{ndvi}'_t|$). The final loss function was obtained by adding the forward loss, ℓ_t , the backward loss, ℓ'_t , and the consistency loss, ℓ_t^{cons}

$$\ell_t^{final} = \ell_t + \ell'_t + \ell_t^{cons} \quad (9)$$

The final prediction at the t -th date was the mean of \widehat{ndvi}_t and \widehat{ndvi}'_t . BRIOS network weights were optimized during training by minimizing the loss function of Equation 9, using the iterative back-propagation with Adaptive Moment Estimation (Adam) algorithm (Kingma and Ba 2014). After each iteration, Adam algorithm updates the weights towards the global minimum of the loss function.

3. Data and experiments

3.1. Testing sites

We tested the BRIOS method on three full Sentinel-2 tiles (approximately 100 km × 100 km for each tile) (Figure 4). The first area, covered by the Sentinel-2 T14SNG MGRS tile, is located on the border of Kansas and Oklahoma in the United States (KO site). The land cover of the site is characterized by grasses and crops. A variety of crops, including winter wheat, herbs, soybeans, and alfalfa, primarily grow from October to the following October. The second area, covered by the Sentinel-2 T55HDB MGRS tile, is located in the Coleambally Irrigation Area (CIA site) in southern New South Wales, Australia. This site has been widely used to test spatiotemporal data reconstruction algorithms (Liu et al. 2019; Zhu et al. 2016), as it is known to have a high degree of landscape heterogeneity, consisting mainly of fragmented crop, grassland, and forest. The third area covered by the Sentinel-2 T50SKE MGRS tile is located in the Henan Province, China (Henan site). The region consists of mountainous areas in the northwest and large plains. The mountains are mainly covered with forests and grasslands. Winter wheat and summer maize are the main crops grown in the plains. On July 20, 2021, a severe flood occurred with obvious land cover changes (Cui et al. 2023; Zhang et al. 2021), making reconstruction of the NDVI time series challenging.

3.2. Sentinel data

We collected optical Sentinel-2A&B surface reflectance (SR) images and Sentinel-1 Level-1 SAR images that were recorded in interferometric wide (IW) swath mode (Ground Range Detected (GRD) products) from the Google Earth Engine (GEE) platform. Table 1 shows the number of

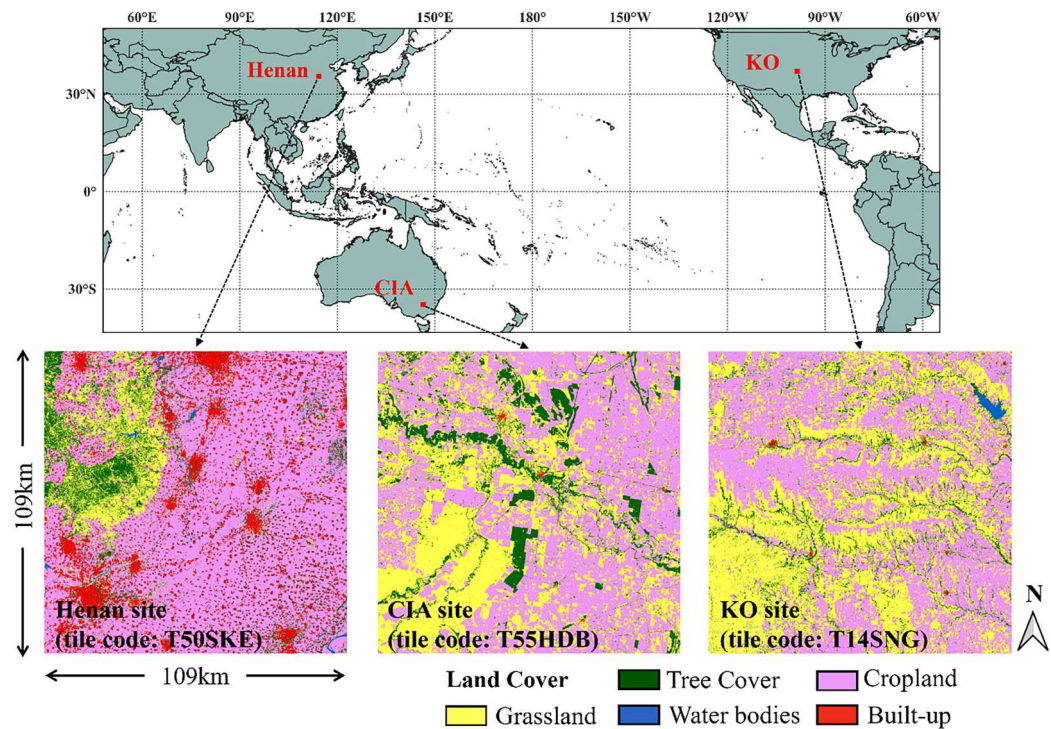


Figure 4. The three Sentinel-2 tiles used as study areas. (a) KO site covered by the T14SNG tile; (b) CIA site covered by the T55HDB tile; and (c) Henan tile covered by the T50SKE. The land cover types for each site shown in the figure were obtained from the ESA WorldCover dataset (Zanaga et al. 2022).

Sentinel 2A&B and Sentinel-1 images at the KO, CIA, and Henan sites that were available during given periods. Only Sentinel-2 images with less than 85% cloud-contaminated pixels are considered. Additionally, only data from one orbit of Sentinel-1 (see Table 1 for each site is either the ascending or descending orbit) can be collected from the ESA website or Google Earth Engine Platform for each study site.

For Sentinel-2A&B images, NDVI data were calculated from the red and near-infrared bands with a spatial resolution of 10 m. Cloud-covered observations were identified by the data quality flags, which are observations with values of 3, 9, or 10 in the Scene Classification flags, or values greater than 65 in the S2_CLOUD_PROBABILITY product (Skakun et al. 2022). For Sentinel-1 SAR images, we followed Mullissa et al. (2021) to generate the backscatter Analysis Ready Data (ARD) using border noise correction, speckle filtering, and radiometric terrain normalization. All processed SAR images were co-registered to match corresponding optical images. We calculated a modified dual-pol Radar Vegetation Index (RVI), given by:

$$RVI = \frac{4\sigma_{VH}^0}{\sigma_{VH}^0 + \sigma_{VV}^0} \quad (10)$$

where σ_{VH}^0 and σ_{VV}^0 are the backscattering intensity of the VH and VV bands (Kim and Van Zyl 2009; Nasirzadehdizaji et al. 2019).

Sentinel-1 and Sentinel-2 data have different imaging dates. To enable identical regular time intervals for the time series of both datasets, we generated an 8-day composited time series for SAR and NDVI data by averaging all available data within each 8-day time interval centered at the composition date (i.e. 8 days before and after the composite date). We used only cloud-free NDVI data for the composition. Gaps may have existed in the composited NDVI time series at some dates when all NDVI observations in the 8-day time period were contaminated by clouds. For the composited SAR data, we first applied spatial mean-filtering with a window size of 7×7 to reduce pepper noise in the SAR image at each composition date, and we then smoothed the composited SAR sequence with a 3-point mean filter. The SG filter was included separately in BRIOS as the feature extractor (described in Section 2.1).

3.3. Training setup

All experiments were carried out on an Intel(R) Core(R) i9-10900 CPU with 10 cores @2.80 GHz with 64GB of RAM and an NVIDIA GeForce RTX 2060 GPU with 6GB GDDR6 memory. To comply with most cases of selecting training data directly from the incomplete NDVI time series data in practical applications, we split one Sentinel-2 tile into training and test datasets as follows (Figure 5). Several cloud-free NDVI observations in Sentinel-2 time-series images were first selected as the validation data, which were removed from the whole NDVI datasets and were not visible to the model. The different scenarios of simulated NDVI gaps are described in Section 3.4. Secondly, the gap-simulated NDVI datasets were then divided into training and test datasets. BRIOS was trained on the training

Table 1. Image information at three study areas.

Study areas	Date Range	Sensor/Tile code	Number
(A) Sentinel-2 image information			
KO	2019/10/01–2020/10/01	Sentinel-2A&B/T14SNG	112
CIA	2020/10/01–2021/10/01	Sentinel-2A&B/T55HDB	115
Henan	2021/01/01–2022/01/01	Sentinel-2A&B/T50SKE	53
(B) Sentinel-1 image information			
KO	2019/10/01–2020/10/01	Sentinel-1 GRD Ascend	115
CIA	2020/10/01–2021/10/01	Sentinel-1 GRD Descend	120
Henan	2021/01/01–2022/01/01	Sentinel-1 GRD Ascend	56

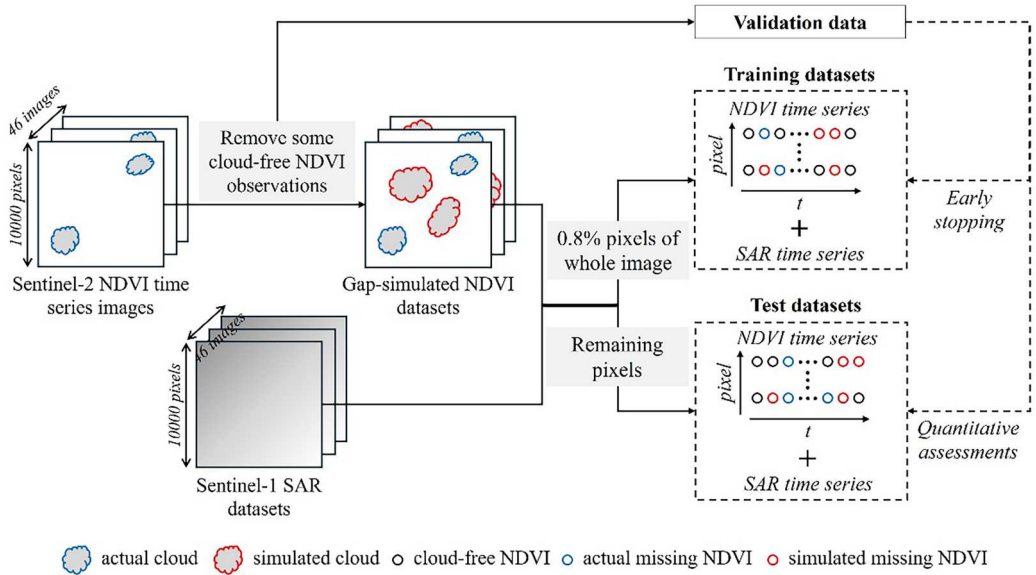


Figure 5. Process of splitting training and test datasets within a Sentinel-2 tile scene. Different scenarios for removing cloud-free NDVI observations are described in Section 3.4.

dataset (800,000 spatially randomly selected pixels, about 0.8% of the total $100 \text{ km} \times 100 \text{ km}$ (10000×10000 pixels) image). For model training, we employed an early stopping strategy to avoid overfitting (Prechelt 2002). This strategy halted training when further improvements on the validation error of simulated NDVI gaps in the training dataset were not observed. Quantitative assessments were performed on the test dataset by comparing the predicted values with the true values simulated as clouds, but actually without clouds, on the entire study areas. Using this method, the training dataset and the simulated data in the test dataset have similar gap settings.

3.4. Comparison of BRIOS and other baseline methods

BRIOS is here evaluated against three popular baseline methods. The first method employs a deep learning model for SAR-optical fusion known as MCNN-Seq, which was proposed by Zhao et al. (2020). The second method is a mono-sensor standard temporal interpolation method represented by Harmonic regression (Belda et al. 2020; Roy and Yan, 2020). The third method, a type of spatio-temporal fusion known as GF-SG, was proposed by Chen et al. (2021). These baseline methods are representative of the prevalent strategies for NDVI time series reconstruction and use varied model inputs. MCNN-Seq processes inputs from both SAR and NDVI datasets for training. GF-SG integrates NDVI data from both Sentinel-2 and MODIS for its data fusion process. In contrast, Harmonic regression only uses Sentinel-2 NDVI.

MCNN-Seq is among the first attempts to enable prediction of NDVI from SAR data based on deep learning model, incorporating a combination of CNN, RNN, and attention modules. 1D-CNN is used to extract robust information from noisy SAR time-series data, and RNN is used to establish the relationship between NDVI and SAR time-series data (Zhao et al. 2020). MCNN-Seq directly estimates NDVI values from SAR time-series data using established functions to convert one to the other. MCNN-Seq is currently the only open-source deep learning model for SAR-NDVI time series fusion and can be obtained from the <https://github.com/kdxiaozi/MCNN-Seq> site.

Harmonic regression is one of the most widely used reconstruction methods to model NDVI time-series observations using a series of harmonic components of different frequencies. After obtaining the coefficients of the frequencies by Ordinary Least Squares (OLS) approach, the

Harmonic model predicts missing NDVI values based on the modeled periodic patterns of vegetation dynamics. In this study, the Harmonic regression method was implemented in the DATimeS software (Beldat et al., 2020). We followed Roy et al. (2020) to use the Fourier1 algorithm in DATimeS and set the number of frequencies parameter to 3.

GF-SG is a filling and filtering method that first fills missing values in the original Landsat (or Sentinel-2) NDVI time series with MODIS NDVI time series and then reconstructs by filtering the synthesized NDVI time series with the weighted SG filter to remove the residual noise (Chen et al. 2021). In this study, the MOD09Q1 NDVI product was used. The source code of GF-SG is available at <https://github.com/ChenY04/GEE.git>. The robustness and efficiency of these methods are evaluated through their ability to reconstruct random and long continuous missing NDVI gaps.

(1) Experiment I : reconstructing random NDVI gaps

We randomly simulated elliptical-shaped clouds on each date of the Sentinel-2 time series to create gap-simulated NDVI datasets. The cloud-free NDVI observations in these simulated clouds were used as ground truth data. Since the spatial distribution and number of cloud pixels in the Sentinel-2 data varies between regions and years, the total number of simulated cloud pixels as a percentage of the total time series images was set to different percentages (i.e. 5%, 10%, 20%, 40%, 60%, and 80%) to simulate the random occurrence of clouds. Figure 6 shows the percentage of missing pixels affected by actual and simulated clouds at each date. The gap-simulated NDVI datasets were then separated into training and test datasets for model training and quantitative evaluations as described in Section 3.3.

(2) Experiment II : reconstructing continuous NDVI gaps

Continuous missing values in NDVI time series are very common in cloudy regions. Therefore, we investigated the performance of different methods under these challenging conditions. In this experiment, it was assumed that all Sentinel-2 images (in both the training and test datasets) are missing for a certain period, and that reconstruction is necessary. At the KO site, the two selected periods were March-April and July-August in 2020 (16 images in total). At the CIA site, the two long gaps were March-April and July-August in 2021 (16 images in total), and at the Henan site, they were February–March and July-August in 2021 (16 images in total). These long gaps were chosen because they corresponded to both the growing season of crops and the cloudy season at the three sites.

3.5. Ablation experiments on BRIOS

To evaluate the effects of NDVI and SAR recurrent architectures on the BRIOS predictions, we trained three recurrent imputation models with our simulated datasets to compare different input data scenarios. The first scenario was our proposed model (BRIOS), relying on two recurrent architectures to integrate both SAR and NDVI input data. The second scenario relied on only optical NDVI input data by removing SAR input data and the corresponding first recurrent architecture from BRIOS (denoted as BRIOS-NDVI) to evaluate whether the SAR-NDVI relationships is beneficial or can be omitted. In the third scenario, NDVI input data were removed from BRIOS. A model with only SAR recurrent architecture (denoted as BRIOS-SAR) was implemented to evaluate the effect of adding the autocorrelation of NDVI to the SAR data. The different scenarios considered the same RNN parameter configurations and were implemented on the NDVI datasets with simulated random gaps (Experiment I) and simulated continuous gaps (Experiment II).

On these two simulated datasets, we conducted another ablation experiment to evaluate the effectiveness of the bidirectional structure and loss. The comparative scenario with BRIOS was the unidirectional recurrent imputation architecture (section 2.2) without a bidirectional loss

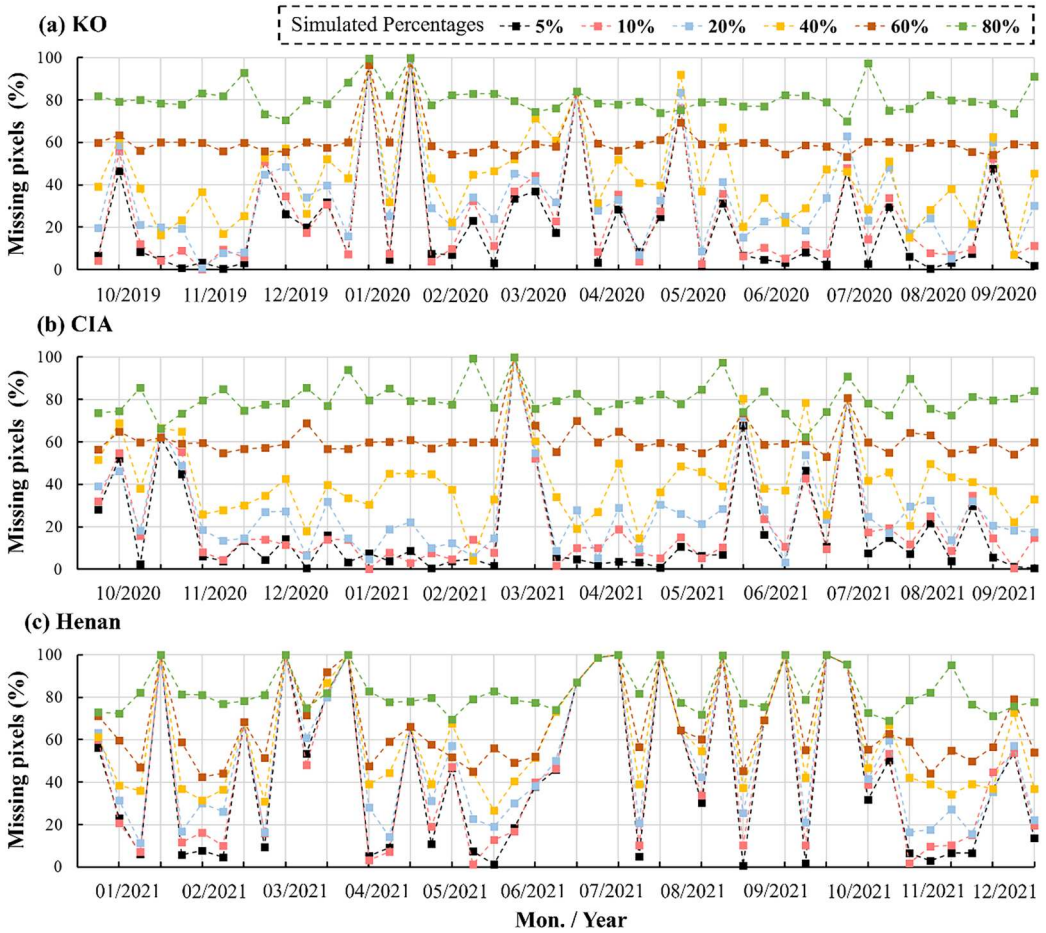


Figure 6. Percentage of pixels affected by actual and simulated clouds for each composite imaging date.

(denoted as RIOS). The different scenarios also considered the same RNN parameter configurations.

3.6. Evaluation indices

Three accuracy evaluation indices were used to evaluate the performance of different methods. The first index was the root mean error (RMSE) defined as:

$$RMSE = \sqrt{\frac{\sum_{i=1}^n (value_{predicti} - value_{truei})^2}{n}} \quad (11)$$

where n represents the total number of cloud-free pixels in the test dataset. The second index was the linear correlation coefficient (R) between the predicted NDVI time series data and the reference NDVI time series data for each pixel in the test dataset. The value of R mainly indicates the consistency of the shapes of different NDVI time series, ranging from -1 to 1. \bar{R} represents the mean R values of all test pixels where NDVI time series without reconstruction are excluded. The

third index was Robert's edge (Edge index), which is defined as follows:

$$\begin{aligned} Edge_{image} &= |D_{ij} - D_{i+1,j+1}| + |D_{ij+1} - D_{i+1,j}|, \\ Edge &= \frac{Edge_{predict} - Edge_{true}}{Edge_{predict} + Edge_{true}} \end{aligned} \quad (12)$$

where D_{ij} is the value of the pixel at the i th row and j th column, and $Edge_{predict}$ and $Edge_{true}$ are the values of the Robert's edge for the predicted image and the reference image, respectively. The Edge index was included in experiment I and II to evaluate the similarity of the spatial contiguity between the predicted and reference cloud-free NDVI pixels. The closer the edge index is to 0, the better is the reconstruction performance.

4. Results

4.1. Assessments for reconstructing random Sentinel-2 NDVI gaps

Figure 7 shows the quantitative assessments of the four methods in Experiment I. BRIOS surpassed the other three methods in terms of RMSE, Edge index and \bar{R} for all scenarios at all sites, followed by GF-SG and Harmonic Regression methods. MCNN-Seq had the lowest accuracy of the four methods. Additionally, all methods showed a decrease in accuracy metrics as the missing percentage increased, but BRIOS stayed relatively stable even for the challenging scenario corresponding to a heavily cloudy situation where 80% of the NDVI was absent. The primary reason for BRIOS's higher accuracy than the interpolation and optical fusion methods (Harmonic and GF-SG) lies in BRIOS using both SAR and NDVI time series as model inputs. This allows the two-layer recurrent architecture in BRIOS to extract long-term vegetation trajectories more effectively than the GF-SG and Harmonic methods, which utilize only NDVI time series as inputs. Despite MCNN-Seq also being a SAR-optical fusion method, its unsatisfactory performance can be attributed to its NDVI prediction relying solely on the long-term trajectory of the SAR time series extracted by a single-layer recursive structure, which might be sensitive to unpredictable fluctuations. This experiment shows that BRIOS is more stable and accurate in large cloudy regions.

4.2. Assessments for reconstructing temporally continuous NDVI gaps

A scenario with temporally continuous NDVI missing values is very common in heavily clouded areas such as subtropical and tropical regions. For this challenging scenario, BRIOS also achieved the lowest RMSE for almost all dates at three sites (Figure 8). The accuracy improvement was more remarkable at periods of significant NDVI increase or decrease, such as the dates in July and August of the crop growing season at the KO site, dates in March marking the beginning of vegetation growth at the CIA site, and dates in July when flooding occurred at the Henan site. Figure 9 shows the average Edge index and spatial distribution of the R -values obtained by different methods. The better Edge index values of BRIOS and the continuity of the spatial distribution of R -values both indicate that BRIOS can effectively reconstruct the spatial details of the landscapes under cloud cover. Moreover, the R -values of BRIOS were higher than the other three methods at all three sites. The improvements were more pronounced at the KO site (average R -value comparison between BRIOS, GF-SG, Harmonic regression, and MCNN-Seq: 0.96 vs. 0.89, 0.84 and 0.41) and the Henan site (average R -value comparison between BRIOS, GF-SG, Harmonic regression and MCNN-Seq: 0.95 vs. 0.88, 0.81 and 0.54). More importantly, BRIOS performed well for almost all land cover types, while the other three methods showed variable performance for different land cover types. Among the three methods, the performance of the MCNN-Seq method was the worst, indicating that it is the least stable and accurate in complex landscapes.

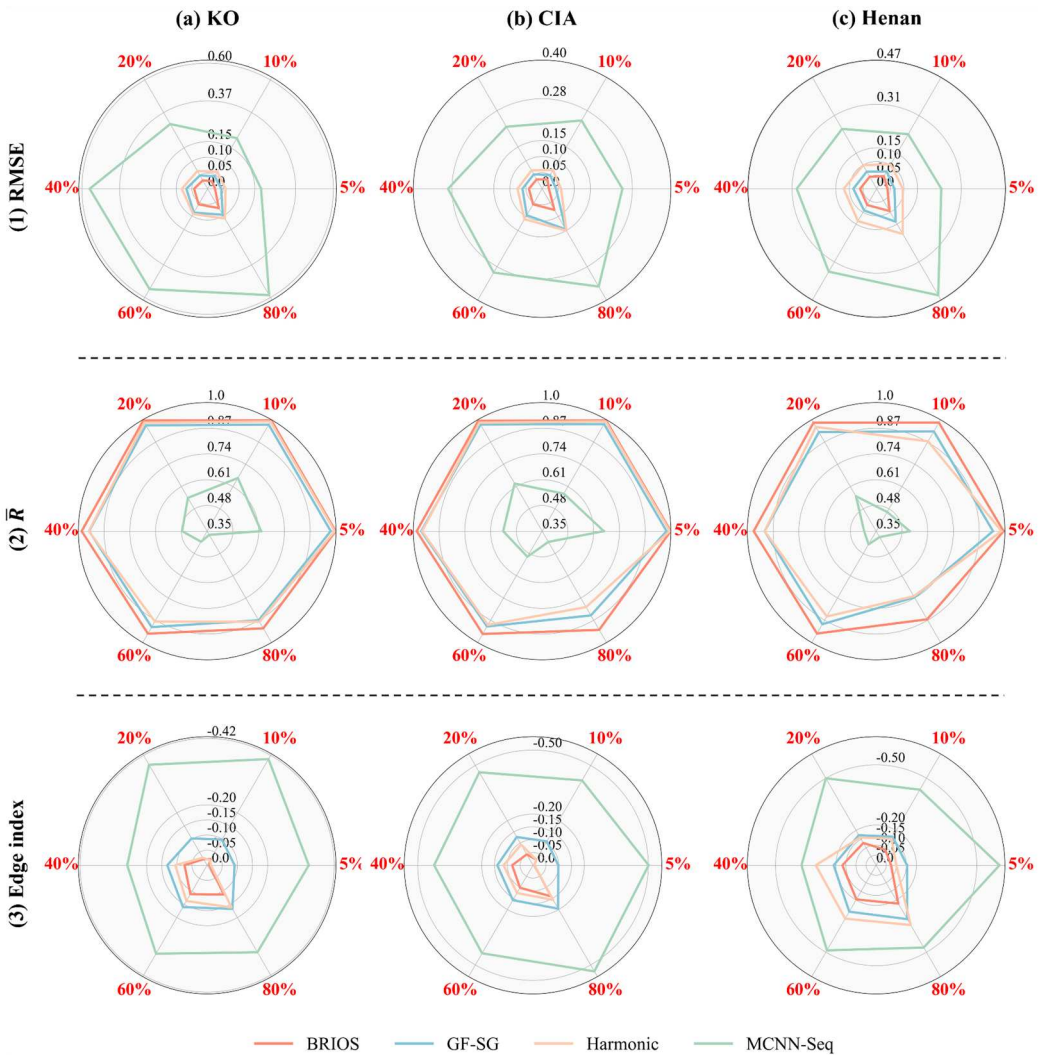


Figure 7. Reconstruction accuracy for different methods in the scenarios where 5%, 10%, 20%, 40%, 60%, and 80% of the valid Sentinel-2 NDVI observations were randomly removed. Here, RMSE, Edge index and \bar{R} -values are the mean values over all test pixels.

For more detailed comparisons, we showed the reconstructed NDVI images on two dates for a small region at the KO site (Figure 10), the CIA site (Figure 11), and the Henan site respectively (Figure 12). In general, the NDVI images predicted by BRIOS captured the spatial details well. The images predicted by GF-SG included overestimated parcels (see Figure 12d) or incorrect spatial details (see Figure 11c,d and Figure 12d), which can be explained by the large difference in spatial resolution between the MODIS and Sentinel-2 NDVI data. The NDVI images reconstructed by Harmonic regression diverged from the actual NDVI images due to the presence of consecutive missing values in the time series, which does not allow for an effective parameterization of the model. We also observed that the NDVI images predicted by MCNN-Seq lost the most spatial detail.

Examples of the reconstructed Sentinel-2 NDVI time-series data for different vegetation classes are shown in Figure 10a,b, Figure 11a,b, and Figure 12a,b. The BRIOS method generally predicted

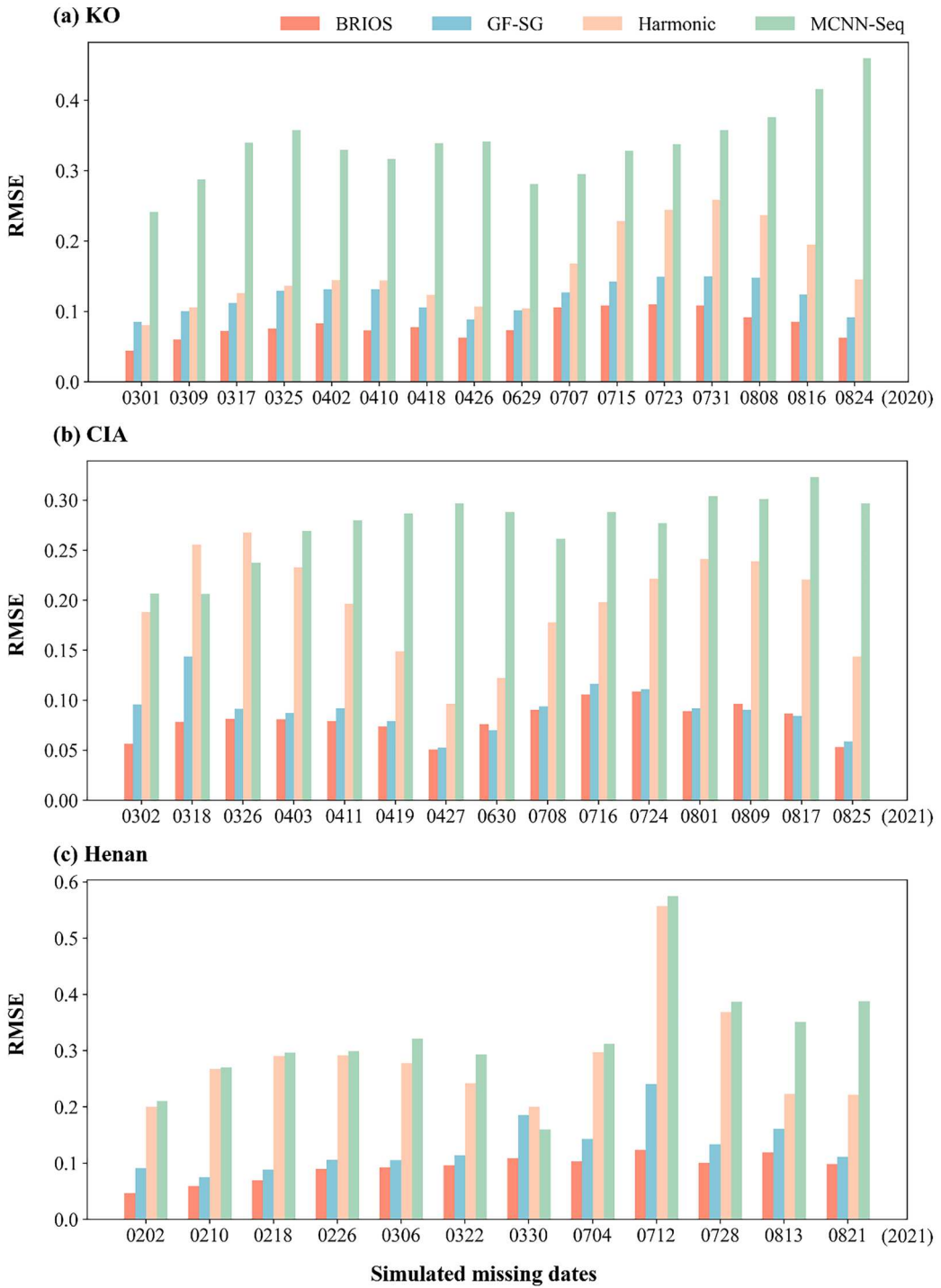


Figure 8. The RMSE values for the simulated continuous dates were derived by comparing the cloud-free NDVI observations with the corresponding predictions from the different methods at the three sites. The dates when no cloud-free NDVI observations were available were excluded.

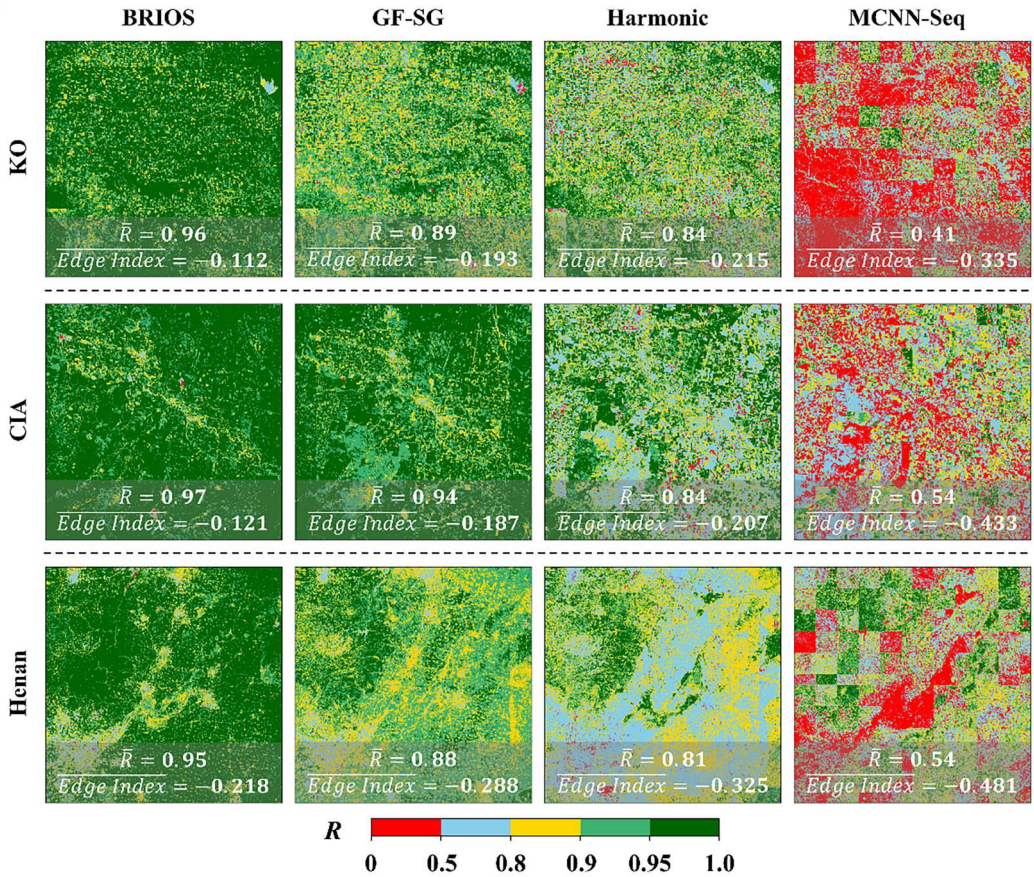


Figure 9. Spatial visualization of the R -values obtained by different methods for the three sites. A five-color map is used to evaluate the defined R -value scale ranges. The R -value of each pixel is calculated based on the similarity between the predicted and actual NDVI time series. Average Edge index is also shown.

vegetation growth well, including the curve for grass, which has a short growing season (Figure 10a), as well as the curve for crop, which has a long growing season (Figure 11b), and multi-cropped cropland (Figure 10b and Figure 12a). In contrast, the GF-SG underestimated the NDVI values in Figure 10a and 10b and overestimated the NDVI values in Figure 12a,b. The Harmonic regression method also underestimated the NDVI values in Figure 10a,b and in Figure 12a,b, and overestimated the NDVI values in Figure 11a,b. All these results indicated that continuous missing values occurring during the key growth periods challenged the performance of both the Harmonic regression method and GF-SG. The MCNN-Seq method again performed the worst, with its reconstructed NDVI time series deviating much more from the NDVI reference values. It should be noted that the BRIOS method more accurately reconstructed the decreased NDVI values affected by the sudden flood in Figure 12b.

4.3. Assessments of ablation experiments

Based on the data from Experiment I (simulated 80% random gaps) and Experiment II (simulated continuous gaps), we conducted ablation experiments with different input variables and corresponding recurrent architectures. As shown in Table 2, BRIOS performed best, followed by BRIOS-NDVI and BRIOS-SAR at three sites. The degradation in the accuracy of BRIOS-NDVI suggests that when many NDVI observations are missing, it is difficult for a single recurrent

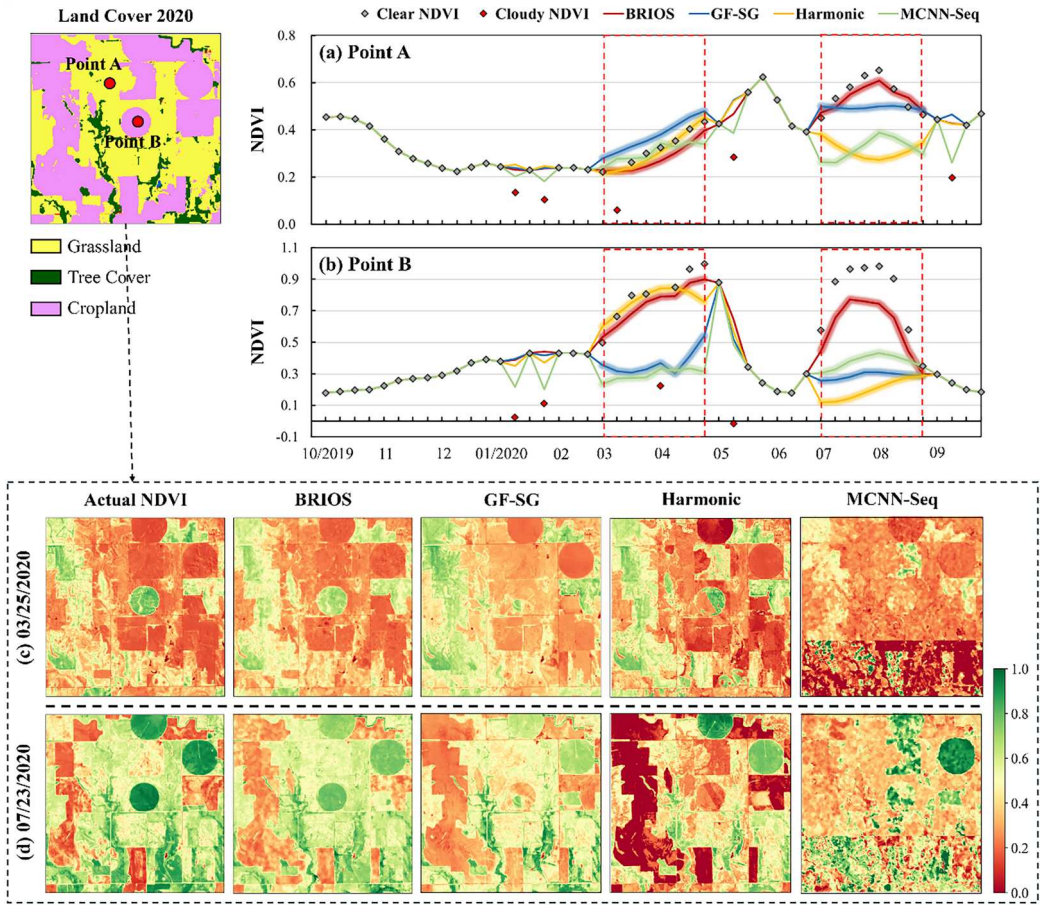


Figure 10. Visual comparisons among different methods at the KO site. (a), (b) are reconstructed Sentinel-2 NDVI time-series data of two vegetation classes (red points in the land cover map from the ESA WorldCover). The red areas in (a) and (b) indicate periods with continuously missing NDVI values. (c), (d) are actual Sentinel-2 NDVI images (acquired on 25 Mar. 2020 and 23 Jul. 2020) and NDVI images reconstructed using different methods.

architecture to accurately capture the full-time trajectory of NDVI during the period of missing data using only discrete cloud-free NDVI observations. Interestingly, the RMSE and R-values decreased more for BRIOS-SAR than for BRIOS-NDVI. This poor performance may be because the relationship between the SAR signal and NDVI is more complex and confounded by many environmental

Table 2. RMSE and \bar{R} -value for the ablation experiments using different input variables at the three sites.

		Experiment I (80% random NDVI gaps)		Experiment II (continuous NDVI gaps)	
		RMSE	\bar{R}	RMSE	\bar{R}
KO	BRIOS	0.0715	0.9170	0.0757	0.9552
	BRIOS-NDVI	0.0908	0.8406	0.1029	0.8992
	BRIOS-SAR	0.1515	0.8144	0.1480	0.8805
CIA	BRIOS	0.0762	0.9259	0.0701	0.9652
	BRIOS-NDVI	0.1096	0.8688	0.0997	0.9273
	BRIOS-SAR	0.1452	0.8388	0.1547	0.8739
Henan	BRIOS	0.0947	0.8644	0.0812	0.9583
	BRIOS-NDVI	0.1264	0.7945	0.1097	0.8945
	BRIOS-SAR	0.1795	0.7714	0.1676	0.8444

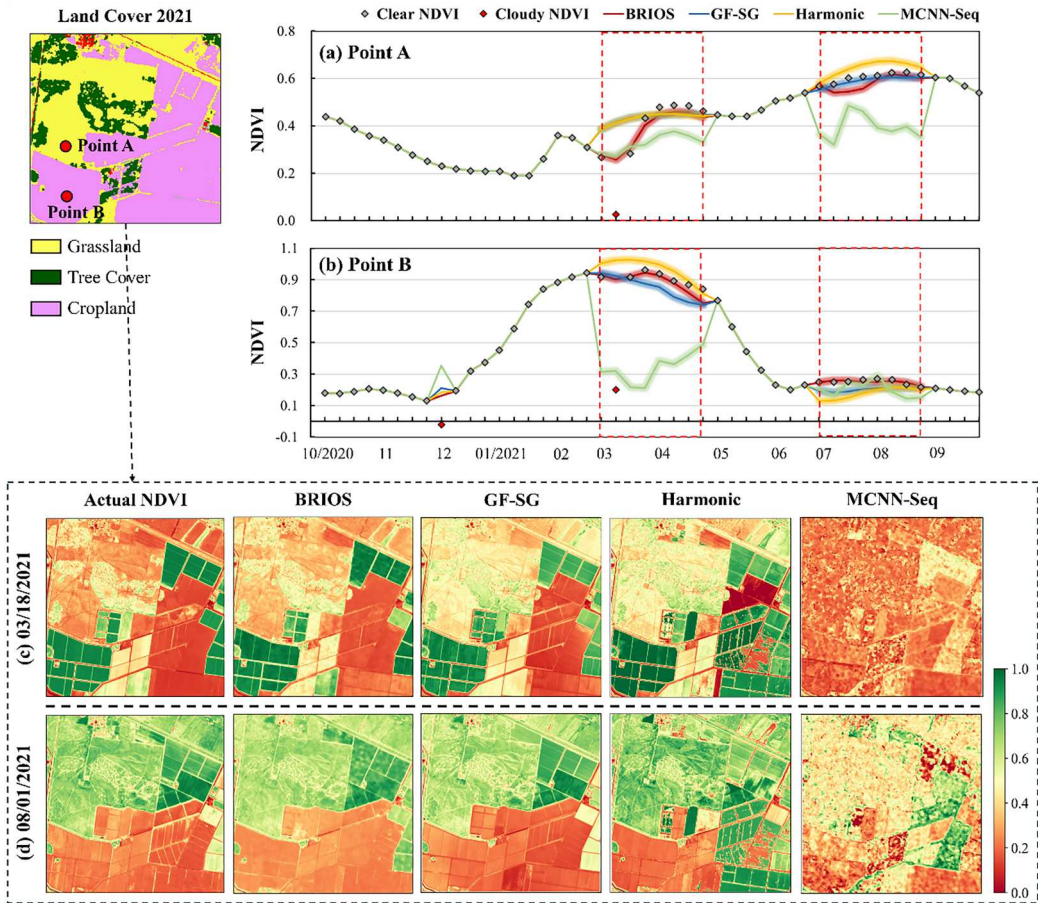


Figure 11. Visual comparisons among different methods at the CIA site. (a), (b) are reconstructed Sentinel-2 NDVI time-series data of two vegetation classes (red points in the land cover map from the ESA WorldCover). The red areas in (a) and (b) indicate periods with continuously missing NDVI values. (c), (d) are actual Sentinel-2 NDVI images (acquired on 18 Mar. 2021 and 1 Aug. 2021) and NDVI images reconstructed using different methods.

factors (e.g. surface humidity, topographic effects, and speckle noise) (Veloso et al. 2017; Vreugdenhil et al. 2018). This may also explain the poor performance of MCNN-Seq in Experiments I and II. These ablation results indicate that NDVI and SAR signals are indispensable and complementary variables as input to BRIOS and that the two-layer recurrent network is better able to integrate the information provided by these two types of data.

The results of ablation experiments with unidirectional structure and bidirectional structure are shown in Table 3. The accuracy of BRIOS was significantly better than RIOS, which indicated that bidirectional structure and loss are helpful in enhancing the model performance. The bidirectional structure can effectively avoid the rapid amplification of early prediction errors as input to the model and the problem of converging slowly.

5. Discussion

5.1. Superiority of BRIOS

The first major advantage is the fusion of SAR and NDVI data as direct inputs within BRIOS. Depending on the data used, previous studies have proposed two types of methods for

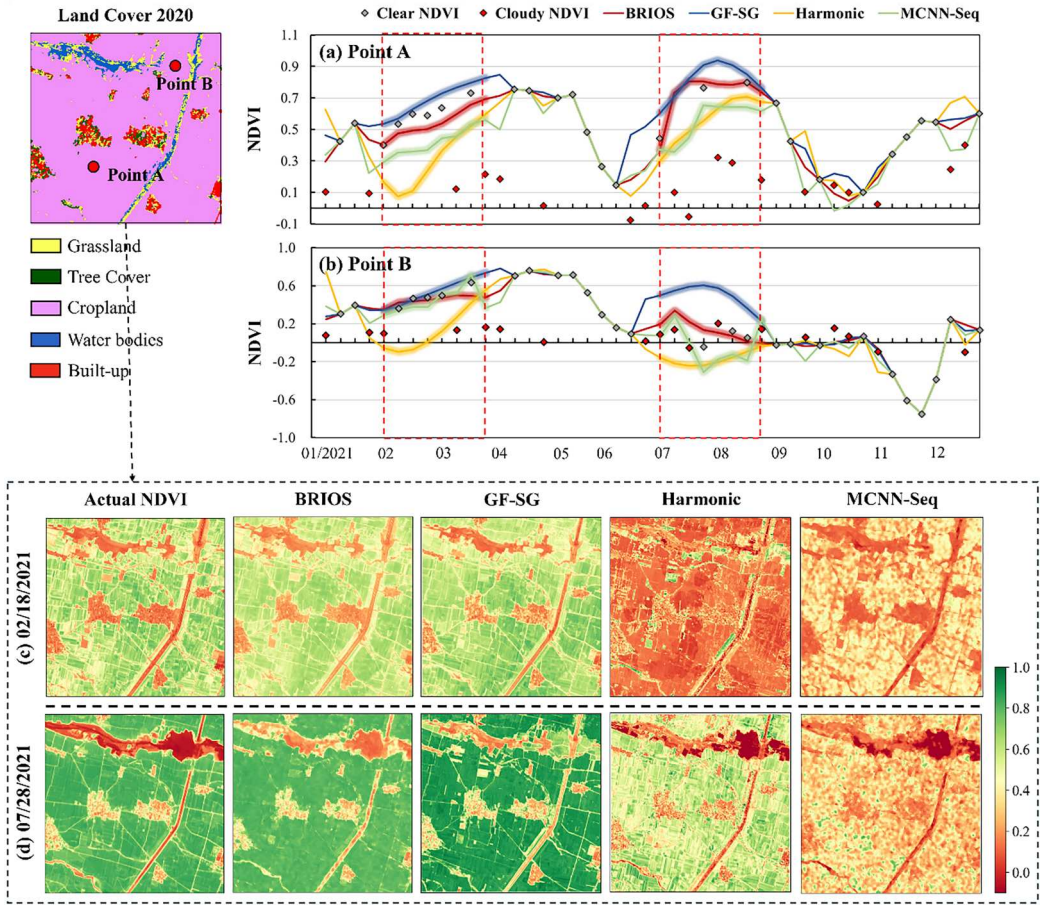


Figure 12. Visual comparisons among different methods at the Henan site. (a), (b) are reconstructed Sentinel-2 NDVI time series of crops without flooding (point A) and those with flooding (point B). The red areas in (a) and (b) indicate periods with continuously missing NDVI values. (c), (d) are actual Sentinel-2 NDVI images (acquired on February 18, 2021, and July 28, 2021, after the July 20 flooding) and NDVI images reconstructed using different methods.

reconstructing high spatial and temporal resolution NDVI time series data, each primarily using either SAR or optical NDVI data. The first group of methods includes temporal interpolation (e.g. harmonic regression) and spatial-temporal fusion (e.g. GF-SG), which mainly exploit the NDVI information by assuming that the missing NDVI values are correlated with discrete, cloud-free NDVI observations. These methods perform well in areas where cloud-free NDVI observations are abundant and relatively uniformly distributed (Yan and Roy, 2020; Chen et al. 2021), but

Table 3. RMSE and \bar{R} -value for the ablation experiments using BRIOS or RIOS at the three sites.

		Experiment I (80% random NDVI gaps)		Experiment II (continuous NDVI gaps)	
		RMSE	\bar{R}	RMSE	\bar{R}
KO	BRIOS	0.0715	0.9170	0.0757	0.9552
	RIOS	0.0892	0.8931	0.0945	0.9203
CIA	BRIOS	0.0762	0.9259	0.0701	0.9652
	RIOS	0.0961	0.9002	0.0894	0.9513
Henan	BRIOS	0.0947	0.8644	0.0812	0.9583
	RIOS	0.1101	0.8294	0.0952	0.9102

may lose their ability to function in heavily cloudy areas or during certain cloudy seasons, as prolonged cloudy weather can affect all optical satellite sensors simultaneously (Chen et al. 2021). The second group of methods is well suited to the problem because they primarily use SAR data with the advantage of penetrating cloud layers. The methods belonging to this group (e.g. MCNN-Seq and SenRVM) focused more on improving the use of temporal SAR information with advanced deep learning networks or on including related environmental ancillary data in the models (e.g. climatic and topographic data). In this case, discrete NDVI observations are used only to compute the loss function, rather than as direct input variables in the models. As a result, previous methods may not be effective when temporal changes of SAR data are inconsistent with those of discrete optical NDVI data due to differences in imaging mechanisms between them and complex environmental interferences. The results of the method comparison and ablation experiments (see the section of results) confirmed that, as with the above analyses, the use of SAR and NDVI data alone has its limitations.

In contrast, the BRIOS model not only attempts to incorporate SAR temporal information but also introduces the use of autocorrelation of NDVI time series. The important role of NDVI time series data has been overlooked in previous deep learning models (Garioud et al. 2021; Zhao et al. 2020). This is the main reason why these models performed the worst in our experiments. In addition to SAR temporal information, there are two advantages to including the autocorrelation features in the discrete NDVI observations. First, the NDVI autocorrelation features can describe the individual temporal shape of vegetation (Cao et al. 2020) for each local area with potentially different environmental status. Second, BRIOS adopts a two-layer recurrent architecture, where one layer focuses on learning the autocorrelation of NDVI time series data, another layer focuses on learning the relationship between NDVI and SAR signals and combines the deep features from the two layers to predict missing NDVI values. This combination helps BRIOS to overcome the fluctuation of SAR signals due to various interferences, which is key to ensuring the establishment of a stable SAR-NDVI relationship and obtaining a good generalization capability over different vegetation types. BRIOS thus learns vegetation change trajectories from both SAR and NDVI data using advanced deep learning networks. Moreover, a bidirectional recurrent imputation model is used in BRIOS to handle time series data in both directions, which enables consistent predictions and avoids a bias-exploding problem (Bengio et al. 2015). These improvements in BRIOS better exploit the separate roles and joint benefits of the Sentinel-2 NDVI and Sentinel-1 SAR signals, resulting in the best performance of the BRIOS model in all of our experiments.

Secondly, the contribution of smoothing the SAR time series in BRIOS should be emphasized. BRIOS extracts the temporal patterns of SAR time series data as input variables to reduce local fluctuations of the SAR time series. The extraction process includes spatiotemporal smoothing and wide-window SG filtering (Section 2.1). To verify the usefulness of this extraction procedure in BRIOS, we further compared the performance of BRIOS with the use of original, composite SAR time series data (referred to as 'BRIOS-Original') and the use of SAR time series data smoothed only by a spatial mean filter and a temporal 3-point mean filter (referred to as 'BRIOS-Smooth'). Figure 13 shows quantitative assessments for the BRIOS-Original, BRIOS-Smooth, and BRIOS scenarios using different SAR input data in Experiment II. As expected, BRIOS-Original performed the worst due to the irregular fluctuations in the original SAR time series. The significant performance improvement was achieved by applying a spatial mean filter and a temporal 3-point mean filter (i.e. BRIOS-Smooth vs. BRIOS-Original), and the performance can be further improved by applying the wide-window SG filter after spatiotemporal smoothing (i.e. BRIOS), suggesting the necessity of extracting temporal change patterns of SAR time series by applying wide-window SG filtering.

5.2. Uncertainty of BRIOS training

As a supervised method, the performance of BRIOS can be influenced by cloud-contaminated NDVI gaps in the training dataset as well as the size of the training dataset. The challenge of

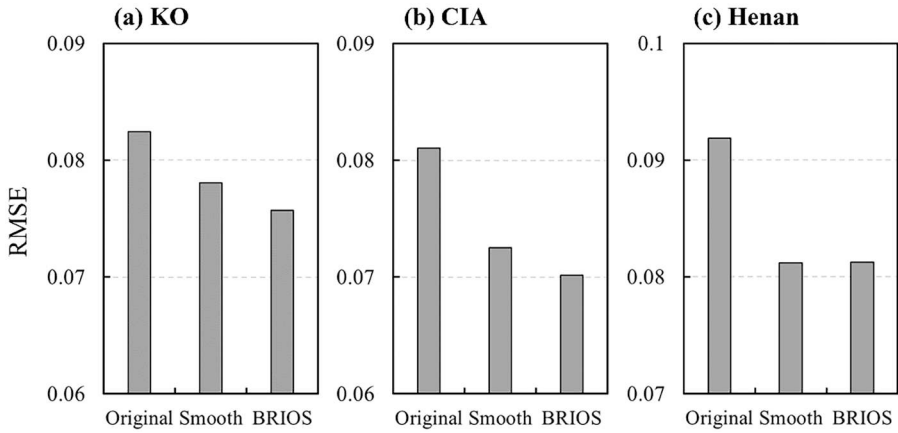


Figure 13. RMSE values of BRIOS when processing the SAR time series in different ways at the (a) KO, (b) CIA, and (c) Henan sites. The *Original*, *Smooth*, and *BRIOS* labels represent the BRIOS-Original, BRIOS-Smooth, and BRIOS scenarios, respectively.

incomplete NDVI series in the training dataset arises due to the randomness of the spatial distribution and the temporal heterogeneity of the cloud contamination on the Sentinel-2 images. As a result, obtaining training data that exactly matches the cloud contamination of the reconstructed region becomes difficult, and this might impede the optimal execution of supervised learning. We employed a new training strategy that simulates cloud contamination on the whole image and then randomly selects training pixels (see section 3.3). This strategy enables us to acquire training data that exactly matches the distribution of cloud contamination in the reconstructed region. We assessed the performance of BRIOS in the different scenarios of randomly simulated NDVI gaps (Experiment I), where incomplete NDVI time series data with different simulated cloud sizes were used as training data. Figure 14 shows the reconstruction accuracy in scenarios with different sizes of simulated NDVI gaps in the training dataset. We also compared the reconstruction accuracy of BRIOS with BRIOS-NDVI, which uses only the autocorrelation of NDVI (details of BRIOS-

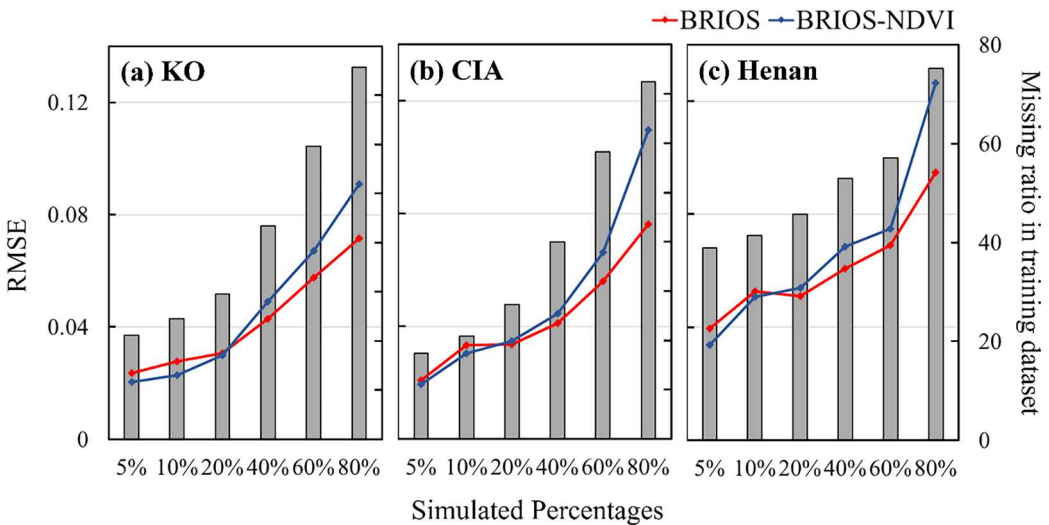


Figure 14. The RMSE of BRIOS (red line) and BRIOS-NDVI (blue line) in the scenarios of different sizes of simulated NDVI gaps in the training dataset. The bar represents the missing ratio of NDVI observations in the training dataset for different scenarios of Experiment I.

NDVI were in section 3.5 of the ablation study). The RMSE values of BRIOS increased less than those of BRIOS-NDVI. The performance of BRIOS-NDVI was more affected by a large number of missing NDVI values in the training dataset than BRIOS. This can be explained by the fact that the use of temporally and spatially consistent quality SAR data reduces the sensitivity of BRIOS to missing NDVI values in the training data, which is difficult to achieve with NDVI data alone. This is also the advantage of BRIOS, whose weights are jointly adjusted according to SAR and NDVI features.

In addition, the effect of training dataset size on BRIOS performance remains unclear. Since BRIOS can handle incomplete NDVI time series, more pixels in one study area, or even all image pixels, can be selected as training data. To explore how the performance of BRIOS is influenced by the training dataset size, we selected a 10 km×10 km subregion at the KO site and carried out a simulation experiment mirroring the methodology of Experiment II. This experiment aimed to reconstruct continuous NDVI gaps using varying sizes of training data. The pixels used for training are 1%, 10%, 25%, 50%, 75%, and 100% of the subregion, respectively. The result in [Figure 15](#) indicates that increasing the size of the training dataset improves the model's accuracy while also prolonging the training duration. Notably, once the training dataset size surpasses 25%, the gains in accuracy begin to plateau, suggesting a diminishing return on further expanding the dataset. Hence, to balance training costs and risks of overfitting, we proposed selectively using a subset of pixels as samples during the training process (e.g. 25% of pixels in a 10km×10 km subregion of a tile). Inspired by this, we also experimented with a training dataset of 800k pixels from the entire Sentinel-2 tile, given that it can describe the higher diversity of landscapes in the whole tile region. We found that the performance of the BRIOS model trained on the 800k pixels of the full Sentinel-2 tile (i.e. BRIOS-800 K) achieved outperformed results for reconstruction in the subregion, with RMSE close to about 0.07 and R-values exceeding 0.95. Considering the trade-off between accuracy improvement and training time, we recommended training and implementing the BRIOS model on an entire Sentinel-2 tile with the training data set comprising 800k random pixels. This is suitable for execution on large-scale areas, tile by tile, and also secures satisfactory results for subregions within a tile scene. With such a training data size, the BRIOS training time for a tile is approximately 5 minutes per epoch, and the reconstruction task of an 8-day interval time series for an entire year on a tile takes roughly 8 hours.

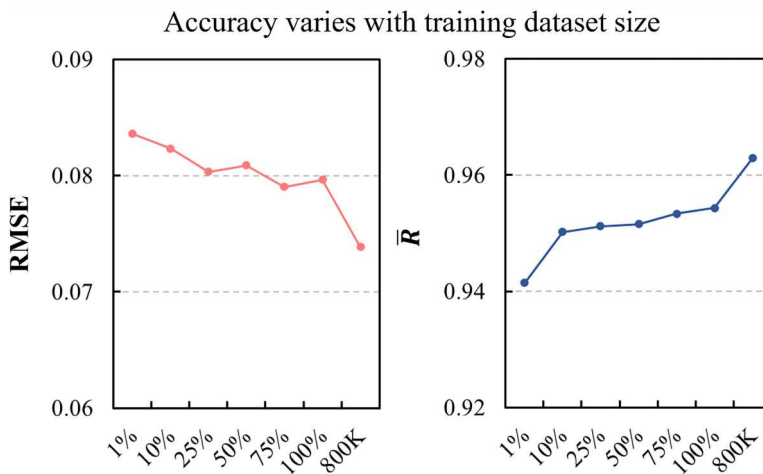


Figure 15. The changes of RMSE and \bar{R} when training BRIOS on different sizes of training dataset. 1%-100% means that 1%-100% random pixels of the subregion are selected as the training dataset. 800k means the BRIOS model trained on the 800k pixels from the entire Sentinel-2 tile.

5.3. The performance of BRIOS in different land cover types

Higher accuracy of BRIOS in Experiment I results confirmed the advantages of BRIOS for reconstructing missing NDVI data with different sizes on three Sentinel-2 tiles with different land cover types. For the reconstruction of continuous NDVI gaps, BRIOS still has advantages in capturing the correct vegetation dynamics. BRIOS can effectively reconstruct various vegetation dynamics, including those with long growing seasons (such as Figure 11a,b), short growing seasons (such as Figure 10a), and multiple growing seasons (such as Figure 10b and Figure 12a). One particular note is the stable performance of BRIOS when sudden land cover changes caused by flooding occur during the missing data period (see Figure 12). In this case, single input methods, constrained by limited information in one input variable, showed reduced accuracy and failed to capture vegetation dynamics. This case also shows that the smoothing operation in BRIOS did not affect the detection of this abrupt change. However, caution should be exercised when using BRIOS to reconstruct sudden and minor vegetation dynamics, as some subtle vegetation changes may be ignored after smoothing operations. For example, the immediate influence of short-term rainfall on vegetation spanning two to three days should be noted. Spatial evaluations were also performed to investigate reconstruction accuracy across different land cover types (see Figure 9). BRIOS exhibited promising results, with R-values consistently above 0.9 for almost all land cover types, except for partial areas with R-values below 0.85 in sparse vegetation cover and wetlands. There is still room to improve BRIOS performance in these areas by including more sparse vegetation and wetland training data.

Additionally, the generalization capabilities of the BRIOS model in real heavily cloudy areas, besides the simulated NDVI gaps, should also be demonstrated. We applied BRIOS to a sub-area of Deyang city located in Sichuan Province, which has an area of about 1094 km² and is covered by multiple vegetation types, such as the rotation between winter wheat and rice in the west and deciduous forests in the central part. We collected all available Sentinel-2 and Sentinel-1 images from 1 January 2021 to 1 October 2021. The percentage of good NDVI observations during 2021 was less than 60% in almost half the regions (see more details in Figure S1 of supplementary materials). Figure 16 shows the reconstructed NDVI images on four dates with heavy cloud coverages (cloud coverages > 50%). The reconstructed results clearly captured the NDVI annual change patterns for different crop types. For example, in the western areas (highlighted by a red rectangle), there are two crop-rotations within a year, either winter wheat-paddy rice or oilseed rape-paddy rice. Correspondingly, the reconstructed NDVI images showed high greenness at two stages (5 March and 14 August) and low greenness after harvesting of the first crops (10 June). In the eastern areas, only one crop (paddy rice) was planted; greenness was thus low in early spring (5 March) for most pixels. Figure 16c further shows the reconstructed continuous NDVI time-series data for a pixel where oilseed rape and paddy rice were rotated. The annual trajectory of the general NDVI was simulated well by BRIOS. A small valley in the NDVI time series during March, which corresponds to the bloom period of oilseed rape (Mercier et al. 2020; d'Andrimont et al. 2020), was also captured by BRIOS.

5.4. Limitations of BRIOS

First, BRIOS was developed here for the reconstruction of the NDVI time series only. As mentioned before, this choice was made based on consideration of the higher correlation between NDVI and SAR data than that between SAR data and reflectance data (Velloso et al. 2017; Villarroya-Carpio, Lopez-Sanchez, and Engdahl 2022). Although theoretically BRIOS can also be applied to other vegetation indices (e.g. EVI2 (Jiang et al. 2008), NDPI (Wang et al. 2017)), biophysical variables (e.g. LAI (Carlson and Ripley 1997), and FAPAR (Gower, Kucharik, and Norman 1999)), the reconstruction uncertainties due to the different mechanisms of these indices should be further evaluated. Secondly, uncertainty in the cloud mask of optical images can reduce the performance of BRIOS. We expect that in the future, as sensor capabilities and cloud detection algorithms improve, more accurate cloud mask data will be produced, which will benefit BRIOS. Thirdly, BRIOS mainly

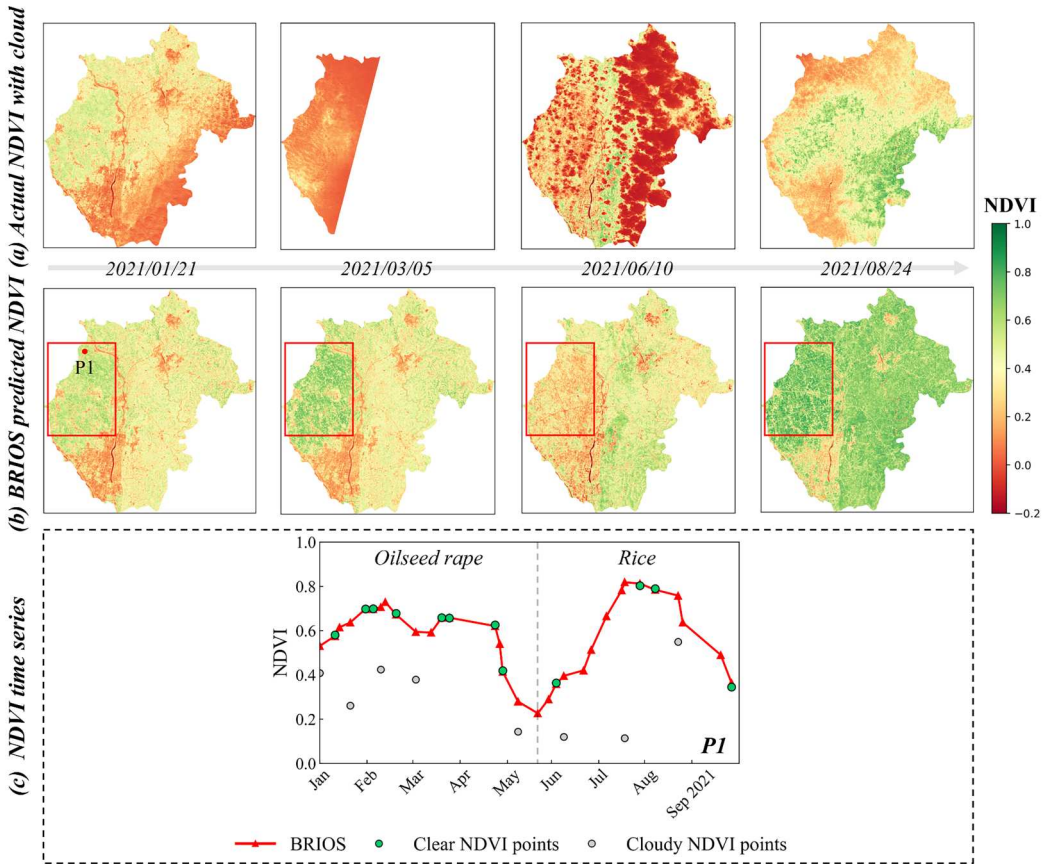


Figure 16. The NDVI images reconstructed by BRIOS for a sub-area in Deyang. (a) Cloud-contaminated Sentinel-2 NDVI images on different dates; (b) NDVI images reconstructed by BRIOS; (c) The reconstructed Sentinel-2 NDVI time-series data for point P1.

considers the fusion of Sentinel-1 and 2 data with the same 10 m spatial resolution. Landsat time series data contain many historical observations and have been widely used for long-term vegetation monitoring. These observations are more likely to be discontinuous due to their 16-day revisit and cloud contamination. How to reconstruct high-quality Landsat time series by fusing with SAR data is also of interest. The challenge of Landsat-SAR fusion may be the different spatial resolutions of the sensors (e.g. 30 m vs. 10 m).

Currently, some new deep learning architectures, such as the Transformers (Vaswani et al. 2017), have emerged and achieved great success in processing sequential data, such as natural language processing (NLP) and image processing (Han et al. 2022). These newly developed models have substantial potential to replace the role of the RNN in BRIOS, although they require more training samples and computational resources. We call for greater efforts to explore this potential, taking into account the two contributions described in Section 5.1.

6. Conclusions

We developed a novel method (called BRIOS) to reconstruct high-quality Sentinel-2 NDVI time-series data. BRIOS employs a two-layer recurrent architecture, where one layer focuses on learning the autocorrelation of NDVI time series data, and another layer focuses on learning the relationship between NDVI and SAR signals, and combines the deep features from the two layers to predict missing NDVI values. By fully exploiting the autocorrelation of NDVI time series data and the

coordination of SAR and NDVI data to establish stable SAR-NDVI relationships, this new BRIOS model outperformed three baseline methods (GF-SG spatiotemporal fusion, Harmonic regression interpolation, and MCNN-Seq deep learning) in our experiments to reconstruct 8-day Sentinel-2 composite NDVI time series data on three full 100km×100 km Sentinel-2 tiles. There are four significant improvements. First, BRIOS is more reliable for reconstructing Sentinel-2 NDVI time-series data with random or long-term, continuous missing values in heavily cloudy areas. Secondly, BRIOS shows impressive generalization capabilities to simulate the NDVI temporal dynamics of varied vegetation types, such as grasses, forests, and crops. It accurately captures short and long growing periods, multi-cropping systems, and abrupt land cover changes. Thirdly, the BRIOS model can flexibly adjust its learning based on the varying sizes of cloud and training datasets, and recommended training settings are available for a Sentinel-2 tile. Fourth, the extraction of temporal change patterns of SAR data by spatiotemporal smoothing and SG filtering is extremely useful for improving the performance of SAR-optical fusion. We expect that BRIOS will popularize the synthesized use of Sentinel SAR and NDVI time series data in ecological, geographic, and environmental studies.

Disclosure statement

No potential conflict of interest was reported by the author(s).

Funding

This research was funded by the 2nd Scientific Expedition to the Qinghai-Tibet Plateau [grant number 2019QZKK0106] and the National Natural Science Foundation of China [grant numbers U23A2018 and 42271379].

Data availability statement

The data that support the findings of this study are available from the corresponding author and the first author upon reasonable request.

References

- Belda, S., L. Pipia, P. Morcillo-Pallarés, J. P. Rivera-Caicedo, E. Amin, C. De Grave, and J. Verrelst. 2020. "DATimeS: A Machine Learning Time Series GUI Toolbox for gap-Filling and Vegetation Phenology Trends Detection." *Environmental Modelling & Software* 127:104666. <https://doi.org/10.1016/j.envsoft.2020.104666>.
- Bengio, S., O. Vinyals, N. Jaitly, and N. Shazeer. 2015. "Scheduled Sampling for Sequence Prediction with Recurrent Neural Networks." *Advances in neural information processing systems*. Montreal, Canada.
- Cao, R., Y. Chen, J. Chen, X. L. Zhu, and M. G. Shen. 2020. "Thick Cloud Removal in Landsat Images Based on Autoregression of Landsat Time-Series Data." *Remote Sensing of Environment* 249:112001. <https://doi.org/10.1016/j.rse.2020.112001>.
- Cao, R., Y. Chen, M. Shen, J. Chen, J. Zhou, C. Wang, and W. Yang. 2018. "A Simple Method to Improve the Quality of NDVI Time-Series Data by Integrating Spatiotemporal Information with the Savitzky-Golay Filter." *Remote Sensing of Environment* 217:244–257. <https://doi.org/10.1016/j.rse.2018.08.022>.
- Carlson, T. N., and D. A. Ripley. 1997. "On the Relation Between NDVI, Fractional Vegetation Cover, and Leaf Area Index." *Remote Sensing of Environment* 62 (3): 241–252. [https://doi.org/10.1016/S0034-4257\(97\)00104-1](https://doi.org/10.1016/S0034-4257(97)00104-1).
- Carrao, H., P. Gonçalves, and M. Caetano. 2009. "A Nonlinear Harmonic Model for Fitting Satellite Image Time Series: Analysis and Prediction of Land Cover Dynamics." *IEEE Transactions on Geoscience and Remote Sensing* 48 (4): 1919–1930. <https://doi.org/10.1109/TGRS.2009.2035615>.
- Che, Z. P., S. Purushotham, K. Cho, D. Sontag, and Y. Liu. 2018. "Recurrent Neural Networks for Multivariate Time Series with Missing Values." *Scientific Reports* 8 (1): 6085. <https://doi.org/10.1038/s41598-018-24271-9>.
- Chen, Y., R. Cao, J. Chen, L. Liu, and B. Matsushita. 2021. "A Practical Approach to Reconstruct High-Quality Landsat NDVI Time-Series Data by gap Filling and the Savitzky-Golay Filter." *ISPRS Journal of Photogrammetry and Remote Sensing* 180:174–190. <https://doi.org/10.1016/j.isprsjprs.2021.08.015>.
- Chen, Y., R. Cao, J. Chen, X. L. Zhu, J. Zhou, G. Wang, M. G. Shen, X. H. Chen, and W. Yang. 2020. "A new Cross-Fusion Method to Automatically Determine the Optimal Input Image Pairs for NDVI Spatiotemporal Data

- Fusion." *IEEE Transactions on Geoscience and Remote Sensing* 58 (7): 5179–5194. <https://doi.org/10.1109/TGRS.2020.2973762>.
- Chen, J., P. Jönsson, M. Tamura, Z. Gu, B. Matsushita, and L. Eklundh. 2004. "A Simple Method for Reconstructing a High-Quality NDVI Time-Series Data set Based on the Savitzky–Golay Filter." *Remote Sensing of Environment* 91 (3–4): 332–344. <https://doi.org/10.1016/j.rse.2004.03.014>.
- Claverie, M., J. Ju, J. G. Masek, J. L. Dungan, E. F. Vermote, J. Roger, S. V. Skakun, and C. Justice. 2018. "The Harmonized Landsat and Sentinel-2 Surface Reflectance Data set." *Remote Sensing of Environment* 219:145–161. <https://doi.org/10.1016/j.rse.2018.09.002>.
- Cui, J., Y. Guo, Q. Xu, D. Li, W. Chen, L. Shi, G. Ji, and L. Li. 2023. "Extraction of Information on the Flooding Extent of Agricultural Land in Henan Province Based on Multi-Source Remote Sensing Images and Google Earth Engine." *Agronomy* 13 (2): 355. <https://doi.org/10.3390/agronomy13020355>.
- d'Andrimont, R., M. Taymans, G. Lemoine, A. Ceglar, M. Yordanov, and M. Velde. 2020. "Detecting Flowering Phenology in oil Seed Rape Parcels with Sentinel-1 and-2 Time Series." *Remote Sensing of Environment* 239:111660. <https://doi.org/10.1016/j.rse.2020.111660>.
- Delbart, N., T. L. Toan, L. Kergoat, and V. Fedotova. 2006. "Remote Sensing of Spring Phenology in Boreal Regions: A Free of Snow-Effect Method Using NOAA-AVHRR and SPOT-VGT Data (1982–2004)." *Remote Sensing of Environment* 101 (1): 52–62. <https://doi.org/10.1016/j.rse.2005.11.012>.
- Ebel, P., A. Meraner, M. Schmitt, and X. X. Zhu. 2020. "Multisensor Data Fusion for Cloud Removal in Global and all-Season Sentinel-2 Imagery." *IEEE Transactions on Geoscience and Remote Sensing* 59 (7): 5866–5878. <https://doi.org/10.1109/TGRS.2020.3024744>.
- Fauvel, M., M. Lopes, T. Dubo, J. Rivers-Moore, P. Frison, N. Gross, and A. Ouin. 2020. "Prediction of Plant Diversity in Grasslands Using Sentinel-1 and-2 Satellite Image Time Series." *Remote Sensing of Environment* 237:111536. <https://doi.org/10.1016/j.rse.2019.111536>.
- Fisher, J. I., J. F. Mustard, and M. A. Vadeboncoeur. 2006. "Green Leaf Phenology at Landsat Resolution: Scaling from the Field to the Satellite." *Remote Sensing of Environment* 100 (2): 265–279. <https://doi.org/10.1016/j.rse.2005.10.022>.
- Gao, F., J. Masek, M. Schwaller, and F. Hall. 2006. "On the Blending of the Landsat and MODIS Surface Reflectance: Predicting Daily Landsat Surface Reflectance." *IEEE Transactions on Geoscience and Remote Sensing* 44 (8): 2207–2218. <https://doi.org/10.1109/TGRS.2006.872081>.
- Gao, J., Q. Yuan, J. Li, H. Zhang, and X. Su. 2020. "Cloud Removal with Fusion of High Resolution Optical and SAR Images Using Generative Adversarial Networks." *Remote Sensing* 12 (1): 191. <https://doi.org/10.3390/rs12010191>.
- Garioud, A., S. Valero, S. Giordano, and C. Mallet. 2021. "Recurrent-based Regression of Sentinel Time Series for Continuous Vegetation Monitoring." *Remote Sensing of Environment* 263:112419. <https://doi.org/10.1016/j.rse.2021.112419>.
- Goodfellow, I., Y. Bengio, and A. Courville. 2016. *Deep Learning*. Cambridge, USA: MIT Press.
- Gower, S. T., C. J. Kucharik, and J. M. Norman. 1999. "Direct and Indirect Estimation of Leaf Area Index, fAPAR, and net Primary Production of Terrestrial Ecosystems." *Remote Sensing of Environment* 70 (1): 29–51. [https://doi.org/10.1016/S0034-4257\(99\)00056-5](https://doi.org/10.1016/S0034-4257(99)00056-5).
- Han, K., Y. Wang, H. Chen, X. Chen, J. Guo, Z. Liu, Y. Tang, et al. 2022. "A Survey on Vision Transformer." *IEEE Transactions on Pattern Analysis and Machine Intelligence* 45 (1): 87–110. <https://doi.org/10.1109/TPAMI.2022.3152247>.
- Huete, A., K. Didan, T. Miura, E. P. Rodriguez, X. Gao, and L. G. Ferreira. 2002. "Overview of the Radiometric and Biophysical Performance of the MODIS Vegetation Indices." *Remote Sensing of Environment* 83 (1-2): 195–213. [https://doi.org/10.1016/S0034-4257\(02\)00096-2](https://doi.org/10.1016/S0034-4257(02)00096-2).
- Jia, L., H. Shang, G. Hu, and M. Menenti. 2011. "Phenological Response of Vegetation to Upstream River Flow in the Heihe River Basin by Time Series Analysis of MODIS Data." *Hydrology and Earth System Sciences* 15 (3): 1047–1064. <https://doi.org/10.5194/hess-15-1047-2011>.
- Jiang, Z., A. R. Huete, K. Didan, and T. Miura. 2008. "Development of a two-Band Enhanced Vegetation Index Without a Blue Band." *Remote Sensing of Environment* 112 (10): 3833–3845. <https://doi.org/10.1016/j.rse.2008.06.006>.
- Kim, Y., T. Jackson, R. Bindlish, H. Lee, and S. Hong. 2011. "Radar Vegetation Index for Estimating the Vegetation Water Content of Rice and Soybean." *IEEE Geoscience and Remote Sensing Letters* 9 (4): 564–568.
- Kim, Y., and J. J. Van Zyl. 2009. "A Time-Series Approach to Estimate Soil Moisture Using Polarimetric Radar Data." *IEEE Transactions on Geoscience and Remote Sensing* 47 (8): 2519–2527. <https://doi.org/10.1109/TGRS.2009.2014944>.
- Kingma, D. P., and J. Ba. 2014. "Adam: A method for stochastic optimization." arXiv preprint arXiv:1412.6980.
- Li, J. B., C. Li, W. Xu, H. Feng, F. Zhao, H. Long, Y. Meng, W. Chen, H. Yang, and G. Yang. 2022. "Fusion of Optical and SAR Images Based on Deep Learning to Reconstruct Vegetation NDVI Time Series in Cloud-Prone Regions." *International Journal of Applied Earth Observation and Geoinformation* 112:102818. <https://doi.org/10.1016/j.jag.2022.102818>.

- Li, S., L. Xu, Y. Jing, H. Yin, X. Li, and X. Guan. 2021. "High-quality Vegetation Index Product Generation: A Review of NDVI Time Series Reconstruction Techniques." *International Journal of Applied Earth Observation and Geoinformation* 105:102640. <https://doi.org/10.1016/j.jag.2021.102640>.
- Liu, M., W. Yang, X. L. Zhu, J. Chen, X. Chen, L. Yang, and E. H. Helmer. 2019. "An Improved Flexible Spatiotemporal DATA Fusion (IFSDAF) Method for Producing High Spatiotemporal Resolution Normalized Difference Vegetation Index Time Series." *Remote Sensing of Environment* 227:74–89. <https://doi.org/10.1016/j.rse.2019.03.012>.
- Mandal, D., V. Kumar, D. Ratha, S. Dey, A. Bhattacharya, J. M. Lopez-Sanchez, H. McNairn, and Y. S. Rao. 2020. "Dual Polarimetric Radar Vegetation Index for Crop Growth Monitoring Using Sentinel-1 SAR Data." *Remote Sensing of Environment* 247:111954. <https://doi.org/10.1016/j.rse.2020.111954>.
- Melaas, E. K., M. A. Friedl, and Z. Zhu. 2013. "Detecting Interannual Variation in Deciduous Broadleaf Forest Phenology Using Landsat TM/ETM+ Data." *Remote Sensing of Environment* 132:176–185. <https://doi.org/10.1016/j.rse.2013.01.011>.
- Mercier, A., J. Betbeder, J. Baudry, V. L. Roux, F. Spicher, J. Lacoux, D. Roger, and L. Hubert-Moy. 2020. "Evaluation of Sentinel-1 & 2 Time Series for Predicting Wheat and Rapeseed Phenological Stages." *ISPRS Journal of Photogrammetry and Remote Sensing* 163:231–256. <https://doi.org/10.1016/j.isprsjprs.2020.03.009>.
- Minh, D. H. T., D. Inenco, R. Gaetano, N. Lalande, E. Ndikumana, F. Osman, and P. Maurel. 2018. "Deep Recurrent Neural Networks for Winter Vegetation Quality Mapping via Multitemporal SAR Sentinel-1." *IEEE Geoscience and Remote Sensing Letters* 15 (3): 464–468. <https://doi.org/10.1109/LGRS.2018.2794581>.
- Mullissa, A., A. Vollrath, C. Odongo-Braun, B. Slagter, J. Balling, Y. Gou, N. Gorelick, and J. Reiche. 2021. "Sentinel-1 SAR Backscatter Analysis Ready Data Preparation in Google Earth Engine." *Remote Sensing* 13 (10): 1954. <https://doi.org/10.3390/rs13101954>.
- Nasirzadehdizaji, R., F. B. Sanli, S. Abdikan, Z. Cakir, A. Sekertekin, and M. Ustuner. 2019. "Sensitivity Analysis of Multi-Temporal Sentinel-1 SAR Parameters to Crop Height and Canopy Coverage." *Applied Sciences* 9 (4): 655. <https://doi.org/10.3390/app9040655>.
- Periasamy, S. 2018. "Significance of Dual Polarimetric Synthetic Aperture Radar in Biomass Retrieval: An Attempt on Sentinel-1." *Remote Sensing of Environment* 217:537–549. <https://doi.org/10.1016/j.rse.2018.09.003>.
- Pettorelli, N., J. O. Vik, A. Mysterud, J. Gaillard, C. J. Tucker, and N. C. Stenseth. 2005. "Using the Satellite-Derived NDVI to Assess Ecological Responses to Environmental Change." *Trends in Ecology & Evolution* 20 (9): 503–510. <https://doi.org/10.1016/j.tree.2005.05.011>.
- Prechelt, L. 2002. "Early Stopping-but When?" In *Neural Networks: Tricks of the Trade*, edited by G.B. Orr and KR. Müller, 55–69. Berlin: Springer Berlin Heidelberg.
- Qiu, Y., J. Zhou, J. Chen, and X. Chen. 2021. "Spatiotemporal Fusion Method to Simultaneously Generate Full-Length Normalized Difference Vegetation Index Time Series (SSFIT)." *International Journal of Applied Earth Observation and Geoinformation* 100:102333. <https://doi.org/10.1016/j.jag.2021.102333>.
- Rao, Y., X. Zhu, J. Chen, and J. Wang. 2015. "An Improved Method for Producing High Spatial-Resolution NDVI Time Series Datasets with Multi-Temporal MODIS NDVI Data and Landsat TM/ETM+ Images." *Remote Sensing* 7 (6): 7865–7891. <https://doi.org/10.3390/rs70607865>.
- Roerink, G. J., M. Menenti, and W. Verhoef. 2000. "Reconstructing Cloud Free NDVI Composites Using Fourier Analysis of Time Series." *International Journal of Remote Sensing* 21 (9): 1911–1917. <https://doi.org/10.1080/014311600209814>.
- Rouse J. J. W., R. H. Haas, D. W. Deering, J. A. Schell, and J. C. Harlan. 1974. "Monitoring the vernal advancement and retrogradation (green wave effect) of natural vegetation." "No. E75-10354. 1974.
- Roy, D. P., and L. Yan. 2020. "Robust Landsat-Based Crop Time Series Modelling." *Remote Sensing of Environment* 238:110810. <https://doi.org/10.1016/j.rse.2018.06.038>.
- Scarpa, G., M. Gargiulo, A. Mazza, and R. Gaetano. 2018. "A CNN-Based Fusion Method for Feature Extraction from Sentinel Data." *Remote Sensing* 10 (2): 236. <https://doi.org/10.3390/rs10020236>.
- Skakun, S., J. Wevers, C. Brockmann, G. Doxani, M. Aleksandrov, M. Batič, D. Frantz, et al. 2022. "Cloud Mask Intercomparison EXercise (CMIX): An Evaluation of Cloud Masking Algorithms for Landsat 8 and Sentinel-2." *Remote Sensing of Environment* 274:112990. <https://doi.org/10.1016/j.rse.2022.112990>.
- Vaswani, A., N. Shazeer, N. Parmar, J. Uszkoreit, L. Jones, A. N. Gomez, Ł. Kaiser, and I. Polosukhin. 2017. "Attention is all you Need" Advances in Neural Information Processing Systems. CA, USA.
- Veloso, A., S. Mermoz, A. Bouvet, T. L. Toan, M. Planells, J. Dejoux, and E. Ceschia. 2017. "Understanding the Temporal Behavior of Crops Using Sentinel-1 and Sentinel-2-Like Data for Agricultural Applications." *Remote Sensing of Environment* 199:415–426. <https://doi.org/10.1016/j.rse.2017.07.015>.
- Villarroya-Carpio, Arturo, J. M. Lopez-Sanchez, and M. E. Engdahl. 2022. "Sentinel-1 Interferometric Coherence as a Vegetation Index for Agriculture." *Remote Sensing of Environment* 280:113208. <https://doi.org/10.1016/j.rse.2022.113208>.
- Vreugdenhil, M., W. Wagner, B. Bauer-Marschallinger, I. Pfeil, I. Teubner, C. Rüdiger, and P. Strauss. 2018. "Sensitivity of Sentinel-1 Backscatter to Vegetation Dynamics: An Austrian Case Study." *Remote Sensing* 10 (9): 1396. <https://doi.org/10.3390/rs10091396>.

- Wang, C., J. Chen, J. Wu, Y. Tang, P. Shi, T. A. Black, and K. Zhu. 2017. "A Snow-Free Vegetation Index for Improved Monitoring of Vegetation Spring Green-up Date in Deciduous Ecosystems." *Remote Sensing of Environment* 196:1–12. <https://doi.org/10.1016/j.rse.2017.04.031>.
- Wang, Q., Y. Ma, K. Zhao, and Y. Tian. 2022. "A Comprehensive Survey of Loss Functions in Machine Learning." *Annals of Data Science* 9: 187–212. <https://doi.org/10.1007/s40745-020-00253-5>.
- Wilson, B. T., J. F. Knight, and R. E. McRoberts. 2018. "Harmonic Regression of Landsat Time Series for Modeling Attributes from National Forest Inventory Data." *ISPRS Journal of Photogrammetry and Remote Sensing* 137:29–46. <https://doi.org/10.1016/j.isprsjprs.2018.01.006>.
- Xiong, C., H. Ma, S. L. Liang, T. He, Y. Zhang, G. Zhang, and J. Xu. 2023. "Improved Global 250 m 8-day NDVI and EVI Products from 2000–2021 Using the LSTM Model." *Scientific Data* 10 (1): 800. <https://doi.org/10.1038/s41597-023-02695-x>.
- Yan, L., and D. P. Roy. 2018. "Large-area gap Filling of Landsat Reflectance Time Series by Spectral-Angle-Mapper Based Spatio-Temporal Similarity (SAMSTS)." *Remote Sensing* 10 (4): 609. <https://doi.org/10.3390/rs10040609>.
- Yan, L., and D. P. Roy. 2020. "Spatially and Temporally Complete Landsat Reflectance Time Series Modelling: The Fill-and-fit Approach." *Remote Sensing of Environment* 241:111718. <https://doi.org/10.1016/j.rse.2020.111718>.
- Zanaga, D., R. V. D. Kerchove, D. Daems, W. D. Keersmaecker, C. Brockmann, G. Kirches, J. Wevers, et al. 2022. "ESA WorldCover 10 m 2021 v200."
- Zeng, Y., D. Hao, A. Huete, B. Dechant, J. Berry, J. M. Chen, J. Joiner, et al. 2022. "Optical Vegetation Indices for Monitoring Terrestrial Ecosystems Globally." *Nature Reviews Earth & Environment* 3 (7): 477–493. <https://doi.org/10.1038/s43017-022-00298-5>.
- Zhang, S., Z. Ma, Z. Li, P. Zhang, Q. Liu, Y. Nan, J. Zhang, S. Hu, Y. Feng, and H. Zhao. 2021. "Using CYGNSS Data to map Flood Inundation During the 2021 Extreme Precipitation in Henan Province, China." *Remote Sensing* 13 (24): 5181. <https://doi.org/10.3390/rs13245181>.
- Zhao, W., Y. Qu, J. Chen, and Z. Yuan. 2020. "Deeply Synergistic Optical and SAR Time Series for Crop Dynamic Monitoring." *Remote Sensing of Environment* 247:111952. <https://doi.org/10.1016/j.rse.2020.111952>.
- Zhou, J. X., J. Chen, X. Chen, X. Zhu, Y. Qiu, H. Song, Y. Rao, C. Zhang, X. Cao, and X. Cui. 2021. "Sensitivity of six Typical Spatiotemporal Fusion Methods to Different Influential Factors: A Comparative Study for a Normalized Difference Vegetation Index Time Series Reconstruction." *Remote Sensing of Environment* 252:112130. <https://doi.org/10.1016/j.rse.2020.112130>.
- Zhou, J., L. Jia, and M. Menenti. 2015. "Reconstruction of Global MODIS NDVI Time Series: Performance of Harmonic ANalysis of Time Series (HANTS)." *Remote Sensing of Environment* 163:217–228. <https://doi.org/10.1016/j.rse.2015.03.018>.
- Zhu, X. L., F. Cai, J. Tian, and T. K. Williams. 2018. "Spatiotemporal Fusion of Multisource Remote Sensing Data: Literature Survey, Taxonomy, Principles, Applications, and Future Directions." *Remote Sensing* 10 (4): 527. <https://doi.org/10.3390/rs10040527>.
- Zhu, X. L., E. H. Helmer, F. Gao, D. Liu, J. Chen, and M. A. Lefsky. 2016. "A Flexible Spatiotemporal Method for Fusing Satellite Images with Different Resolutions." *Remote Sensing of Environment* 172: 165–177. <https://doi.org/10.1016/j.rse.2015.11.016>.
- Zhu, Z., C. E. Woodcock, C. Holden, and Z. Yang. 2015. "Generating Synthetic Landsat Images Based on all Available Landsat Data: Predicting Landsat Surface Reflectance at any Given Time." *Remote Sensing of Environment* 162:67–83. <https://doi.org/10.1016/j.rse.2015.02.009>.